

Microstructure of Zirconium Alloys and Effects on Performance

Authors

Friedrich Garzaroli
Fürth, Germany

Ron Adamson
Fremont, CA, USA

Kit Coleman
Ontario, Canada



A.N.T. INTERNATIONAL®

© November 2015

Advanced Nuclear Technology International
Analysvägen 5, SE-435 33 Mölnlycke
Sweden

info@antinternational.com
www.antinternational.com

Disclaimer

The information presented in this report has been compiled and analysed by Advanced Nuclear Technology International Europe AB (ANT International®) and its subcontractors. ANT International has exercised due diligence in this work, but does not warrant the accuracy or completeness of the information.

ANT International does not assume any responsibility for any consequences as a result of the use of the information for any party, except a warranty for reasonable technical skill, which is limited to the amount paid for this assignment by each ZIRAT/IZNA programme member.

Contents

1	Summary	1-1
2	Introduction	2-1
3	Techniques for microstructural investigation	3-1
4	Alloys and microstructure	4-1
4.1	Capture cross-section: the dominating property	4-1
4.2	Zirconium alloying guidelines	4-1
4.3	Phase diagrams in zirconium alloys	4-2
4.3.1	Zr-O system	4-3
4.3.2	Zr-Sn system	4-4
4.3.3	Zr-Nb system	4-5
4.3.4	Zr-Fe system	4-6
4.3.5	Zr-Cr system	4-7
4.3.6	Zr-Ni system	4-8
4.3.7	Postscript	4-8
5	Fabrication Processes	5-1
5.1	First stages	5-1
5.2	Mostly α -alloys	5-3
5.3	$(\alpha+\beta)$ -alloys	5-7
6	Slip and twinning systems during plastic deformation	6-1
6.1	Unirradiated material	6-1
6.2	Irradiated material	6-5
7	Texture and Anisotropy	7-1
7.1	Texture	7-1
7.2	Anisotropy	7-8
8	Deformation	8-1
8.1	Types of deformation during fabrication	8-1
8.1.1	Cold work	8-1
8.1.2	Warm work	8-2
8.1.3	Hot work	8-3
8.2	Grain size and shape after various fabrication steps	8-4
8.3	Effect of cold work and grain size and shape on properties	8-6
9	Second phase particle (SPP)	9-1
9.1	Kind, size and distribution of SPPs	9-1
9.2	Irradiation effects on SPPs	9-10
9.3	SPP Effect on performance	9-23
10	Hydrides and their effect on properties	10-1
10.1	Hydride phases and solubility limits	10-1
10.2	Movement of hydrogen	10-4
10.2.1	Hydrogen concentration gradient	10-4
10.2.2	Temperature gradient	10-4
10.2.3	Stress gradient	10-5
10.2.4	Alloy gradient	10-6
10.3	Stress reorientation	10-7
10.4	Consequence of hydrides on mechanical properties	10-9
10.4.1	Tensile and fracture properties	10-9
10.4.2	Time dependent cracking	10-10

11	Irradiation induced changes of the crystal structure	11-1
12	Effect of irradiation on properties	12-1
12.1	Mechanical properties	12-1
12.2	Irradiation growth and creep	12-6
12.2.1	Irradiation growth	12-6
12.2.2	Creep	12-11
13	Conclusions	13-1
14	References	14-1
	Nomenclature	
	Unit conversion	

1 Summary

This Special Topical Report (STR) reviews microstructural features that contribute to, and in many cases control, safe and efficient operation of reactor core components. Zirconium alloys, in addition to providing low neutron absorption, must be fabricable, have adequate strength, ductility and corrosion resistance, and must ensure predictable in-reactor dimensional stability. Microstructure is important in each area.

Key microstructure features are revealed and characterized by standard techniques, starting with light (often called optical) metallography and including transmission and scanning electron microscopy (TEM and SEM), x-ray diffraction, and a variety of other more modern methods.

Proper alloying, usually based on years of research and testing, provides the base for all the metallurgical and performance characteristics that are needed.

Fabrication processes are key, not only for financial considerations, but for meeting component design, assembly and performance requirements. It is during fabrication where target microstructural features are established and maintained:

- grain size and shape,
- second phase distribution,
- second phase precipitate (SPP) size and distribution,
- residual cold work and dislocation density,
- crystallographic texture and anisotropy.

Second phase precipitates (SPPs) in all the Zr-alloys are important due to their influence on corrosion behaviour, fracture toughness and, perhaps, strength and irradiation growth. The stability of SPPs under irradiation depends on their type and size, and is the subject of continuing research. Light (optical) metallography reveals their general size and distribution, but details on in-reactor SPP stability require careful TEM and EDX (energy dispersive x-ray spectroscopy) analyses.

Zirconium hydrides, formed as part of the corrosion reaction with water, are brittle, and pose a threat to structural integrity of components during in-reactor service and out-of-reactor handling and storage situations. Hydride microstructural features are easily revealed by standard light (optical) metallography or SEM using back scattered electrons. Understanding their characteristics requires use of more advanced techniques, such as diffraction using intense x-ray beams produced in a synchrotron.

Unique microstructure features are produced by irradiation of zirconium alloy components in the reactor:

- Dislocation loops having specific crystallographic orientations are formed. Loops have significant effects on strength, ductility, and dimensional stability.
- Existing SPPs are caused to dissolve or become amorphous, or both. This behaviour significantly affects corrosion, hydrogen pickup and, perhaps, irradiation growth.
- Secondary precipitation and transfer of alloying elements from one phase to another occurs. These phenomena can significantly affect corrosion and hydrogen pick-up.

Details of all these microstructural features introduced in this section are described in this STR.

Light metallography is usually the first technique or tool used by metallurgists to determine the underlying metallurgical structure that controls the macroscopic properties of a material. By using heat tinting, anodization or polarized light, colour contrasts can be produced to differentiate features such as grain size and shape. Etching of the polished surface with specific chemicals brings out various phases such as hydrides, impurities and second phase precipitates (SPPs). An example is given in Figure 2-2. This STR contains many photomicrographs produced by light microscopy.

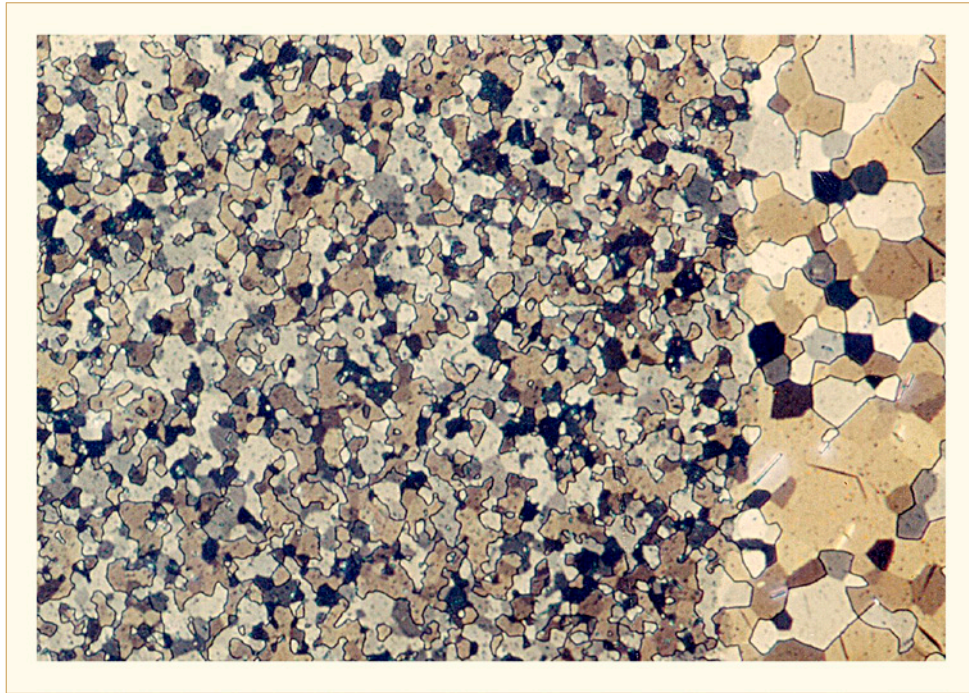


Figure 2-2: Cladding cross-section showing fine grained Zircaloy and large grained zirconium, section polished, etched, anodized, polarized light (magnification about 333X).

In addition, fracture surfaces reflect the microstructure related to failed components. Such microscopy, created in either in 2 or 3 dimensions in the Scanning Electron Microscope (SEM), very usefully complements light microscopy and other techniques to be discussed; however, fractography is beyond the scope of the current STR. A good summary of fractography can be found in Section 2.4 of ZIRAT18/IZNA13 Special Topic Report (STR) “Mechanical Testing of Zirconium Alloys, Volume 1” [Adamson et al, 2013]

Microstructural features of interest to zirconium alloys include

- grain size and shape, including twins
- dislocation density and distribution
- second phase precipitate (SPP) size, distribution and chemical composition
- impurity identification and distribution
- radiation damage features such as dislocation loop type, size and distribution
- hydride concentration and distribution
- alloy phase distribution
- surface features such as oxides and fret-marks.

3 Techniques for microstructural investigation

Quantifying relevant aspects of microstructure requires use of analytical devices, some as old as light (or optical) microscopes and as new as 3D atom probes. Table 3-1 outlines various sophisticated techniques used to investigate various phenomena.

The following is extracted liberally from “Analytical Techniques for Zr Alloy Microstructure”, written by Clément Lemaignan for ZIRAT16/IZNA11 Annual Report, 2011 [Adamson et al, 2011]. The interested reader is urged to refer to that excellent report for details.

As already discussed, microstructure is defined as the structure at the microscopic scale. The structure of a metal or alloy describes how the parts of the piece relate to each other, how they are “assembled”. The microscopic scale is the one that requires a magnification device to be observed, and is conventionally defined as what is observed at a 25 x scale. Therefore the techniques related to naked eye observation (macrostructure) or assemblies, will not be covered in this section. Similarly the subatomic scale remains outside the scope of this section

In metallurgy, knowledge of the microstructure is a mandatory requirement, and has always been requested with the highest accuracy possible. At the beginning of metallurgical investigation, optical (light) microscopy and X-ray diffraction were used as routine tools. Modern techniques such as transmission electron microscope (TEM), neutron diffraction and atomic chemistry tools (SIMS, 3D tomography) are also used but are not routine during fabrication of components, to be described later.

The properties of zirconium alloys are strongly microstructure dependent. With the same composition, the microstructure of an alloy can be markedly changed, depending of its thermomechanical history. Heat treatments, mechanical processing, and conditions of use (a very important point because the effects of irradiation induce major changes in the microstructure, producing large changes in all the properties). Engineering properties, such as mechanical strength, fracture toughness, corrosion resistance, and creep are known to depend on the microstructure.

Bridging a link between the microstructure and the properties allows scientists to understand the mechanisms involved in the control of the property under consideration. This correlation opens the route to improvements in the properties of the alloys and allows the designers to forecast changes in properties during operation (e.g. irradiation hardening or growth, changes in corrosion resistance after heat treatments...).

The question to be answered with respect to the microstructure is to know what are the “parts” to be considered in the way they “relate to each other”. For the microstructures of interest, three major features have to be considered:

- Crystals are the elementary units of metals and alloys. One has to know what is the crystallographic structure (crystallographic system, composition...), what is the shape of each crystal (elongated, equiaxed...), what is their relative orientation (occurrence of a crystallographic texture...).
- Within the crystals, the defects have to be described accurately. Among them, we have to consider chemical defects such as clusters of foreign or solute atoms, linear defects (dislocations) and point defects (irradiation defects such as interstitials or vacancies, or chemical defects – substitutional or interstitial impurities) and planar defects (grain and twin boundaries).
- At the atomic scale, the exact chemical state and chemical environment of each atom controls its behaviour. Of interest are the oxidation state, the surrounding atoms controlling the vibration modes and therefore their mobility, allowing interaction with defects and other atoms leading to segregation and precipitates.

2 Introduction

Microstructure, as the word suggests, is the small scale structure of a zirconium alloy that usually cannot be seen by the eye alone. Although invisible at a macro-scale, microstructure has a dominating effect on most of the performance-related macro-properties of a reactor component: strength, ductility, hardness, toughness, corrosion resistance, dimensional stability (creep, irradiation growth). Even properties normally thought of as physical or chemical properties, such as neutron absorption cross section, thermal expansion, lattice parameter, can be influenced by microstructure.

Although “micro” is generally associated with the prefix¹ 10^{-6} , observation of microstructure generally starts at a magnification of about 25X, which can easily be obtained by a standard laboratory optical (or more properly, light) microscope, up to about 1000X. Higher magnification, resolution, and depth (below the metal surface) of information obtained depend on the wavelength and energy of the probing particle or wave. Ordinary metallography, using light with wavelength near 8×10^3 Angstroms (8×10^4 nm) and energy near 1ev, (see Figure 2-1) produces images of the surface layer only. Such “micrographs” are almost always of highly polished, and sometimes etched, surfaces.

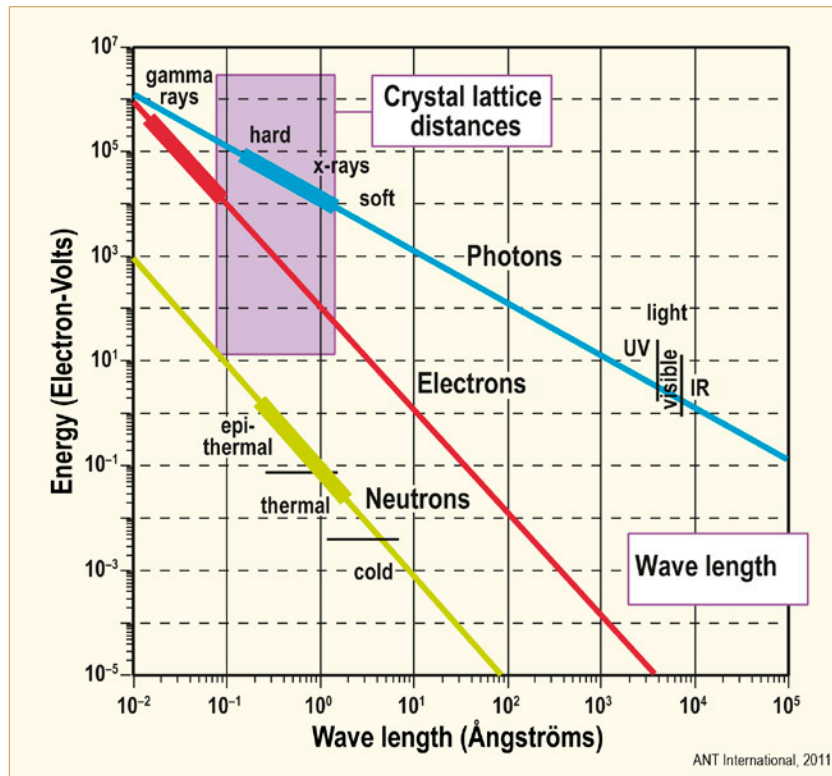


Figure 2-1: Wavelength of the particle as a function of energy of the particle (1 nm = 10 Angstroms).

¹ deci, 10^{-1} ; centi, 10^{-2} ; milli, 10^{-3} ; micro, 10^{-6} ; nano, 10^{-9}

Any physical phenomenon whose characteristic parameters would be affected, in any possible way, by the microstructure will lead to results affected by the microstructure, and therefore could be used for its analysis. Since “Any physical property or quantity measurable in a system is related, in one way or another, to all the other variables of the system” [Avril, 1974], one can consider that any physical phenomenon could be used for the analysis of the microstructure of alloys. Practical considerations limit the techniques of actual interest. Accuracy, selectivity, uniqueness of the relationship between the parameter to be analysed and the microstructure and the output of the physical experiment, or cost or complexity of the measurements limit the list to a set of basic phenomena.

Sorting the different techniques used in metallurgy for the knowledge of the microstructure is a rather difficult task for the reason that any phenomenon that could give any information could be used, at least a-priori. We will limit ourselves to the techniques for which a common agreement exists on the interest, the applicability and the usefulness.

With respect to the physical basis of the physics of concern, the techniques could be categorised as follows:

- Direct measurement of each atom, giving its mass, chemistry and location in the sample. This category includes the secondary ion mass spectroscopy (SIMS), and the 3D atom microprobe.
- Diffraction induced by the periodic (crystallographic) nature of the grains. Any beam whose wavelength is commensurate with the interatomic distance will exhibit diffraction phenomena. X-rays, electrons and neutrons can be used for this purpose. Low angles diffraction will also be described in this section.
- Interactions of particles with the atoms, either in-elastically or elastically:
 - Transmission electron microscope (TEM), and analysis in the TEM by electron energy loss spectroscopy (EELS),
 - Electron probe micro-analysis (EPMA),
 - Neutron radiography,
 - All the nuclear microprobe techniques, including Proton induced X-ray emission (PIXE),
 - Phenomena driven by inelastic interactions, such as the surface imaging obtained by scanning electron microscopy (SEM).

Another group of techniques is based on the change in reaction of an atom to an external excitation, according to its chemical environment. X-ray absorption near the characteristic, absorption energies: Extended X-Ray Absorption Fine Structure (EXAFS) and variant such as X-Ray Absorption Near Edge Spectroscopy (XANES). The dependence of the vibration frequencies of an atom with its environment can be analysed indirectly with infrared photons, such as the Raman spectroscopy, or with γ -rays (Mössbauer spectroscopy).

Table 3-1 and Table 3-2 give details of various techniques and recommendations for investigating specific phenomena.

Table 3-1: Comparison of the different techniques used in alloy microstructure analysis.

Technique	Aim	Samples	Type of information	Operational aspects	Potential limitations
Chemistry					
SIMS Secondary Ion Mass Spectrometry	In depth profile and surface composition of atoms and isotopes	Limited preparation. Sample size ~ cm ² . Analysis depth up to 2 μm. Deeper analysis on tapered sections.	Time evolution of the different isotopes (e/m separation) versus erosion time. Resolution: ~ μm in location, ~ 5 nm in depth, decreasing with erosion depth. Very high dynamics: 10 ⁵ in concentration differences: impurity detection, segregations.	Rather expensive equipment, not present in all the metallurgy labs. Several services available on commercial basis. Few hours per depth profile.	Light elements (H, He) may be contamination from vacuum chamber. Depth limitations due to erosion time and roughening of the erosion crater. Request to convert time in depth (erosion rates?).
3D atom probe	Exact chemistry and location of all the atoms in a given (very small) volume.	Very sharp needle. (radius < 100 nm, length ~ 5 mm) prepared by electropolishing or focused ion beam (FIB) difficult and critical. Need to be conductive material.	Within the volume analysed (10*10*100 nm max.), location and isotope description of all the atoms (e/m separation).	Only a few pieces of equipments per continent. The experiments have to be performed by the teams having such equipment.	Vacuum chamber light elements (H, He) contamination. Collection of the atoms: missing atom ratio unknown. The area analysed may not be representative of the sample. Very large amount of data. Would need procedures for data reduction.
Nuclear microprobe	Determine in depth the concentration of given isotopes, having very specific nuclear reactions.	No preparation. Size: a few cm ² . Possibility to analyse radioactive materials in dedicated installations.	Depth concentration of a given isotope, which is very specific for a nuclear reaction occurring with high-energy incident ion beam.	Only a few installations worldwide! Complex extraction of the physics out of the raw data (straggling, multiple reaction, variation of interaction cross sections with energy). Requires an efficient support from the guest lab.	Only a limited set of reaction of interest and therefore of profiles to be obtained. Difficult access to the equipment: request for proposal, travel to the facility, need of a strong scientific support from the local staff.
EXAFS/XANES X-ray Absorption Fine Structure/X-ray Absorption Near Edge Spectroscopy	Describe the environment of all the atoms of a given species under the X-ray beam.	Has to be thin enough for the beam to pass through, or use fluorescence operation. Depth of analysis below 10 μm.	Raw data is the transmittance of the sample versus X-ray energy. Interpretation of these results in term of local chemistry is not unequivocal. Will analyse all the atoms of the same species. Not phase or gradient separation, only integral or averaged behaviour.	Most of the experiments performed on synchrotron facilities: Formal request of beam times. Many samples can be tested in a few minutes. Excellent support of these installations allows correct interpretation of the results.	Cannot be used without clear expectation of what could be the results. Hypothesis of the suspected environment have to be limited, and a selection will be possible. If configuration is too open, nothing good will come out.

ANT International, 2011

Table 3-1: Comparison of the different techniques used in alloy microstructure analysis. Cont'd

Technique	Aim	Samples	Type of information	Operational aspects	Potential limitations
Chemistry					
Diffraction X-ray	Interatomic distances and crystallographic information. Phase identification.	No limitation. Analysis performed on planar surface, or powders for ceramics. Powerful beams can be used in transmission through about 2 mm.	Intensity vs. diffraction distances. Has to be converted in crystallographic description: cell structure, texture, stresses.	Standard equipment available in any metallurgy laboratory. A few hours per sample. Advance measurements with synchrotron limited availability, but much faster.	Penetration depth below 10 μm (except with synchrotron). Calibration procedures have to be done rigorously.
Diffraction neutrons	Same as above	No preparation. Analysis on the bulk of the sample (a few mm^3) Analyse can be performed on minor phases (<1 vol.%)	Same as above, but in bulk.	Request of a neutron beam (pool reactor, spallation source). Long exposition times (hours to days). Specific elements may inhibit the possibilities (H: diffusion, or B: absorption).	Difficult access to the equipment: request for proposal, travel to the facility, but high local scientific support.
TEM Transmission electron Microscopy	Imaging of the microstructure at high magnification. Local chemistry and crystallography at the same scale.	Disk (\varnothing 3 mm, 0.1 μm for electron transparency) Not too difficult for bulk alloy samples (electrochemical thinning). Difficult, but very valuable samples by FIB preparation.	High contrast on the microstructure: grain size and shape, crystallography, orientation, local element concentrations. Resolution near atomic size. Usually combination of the three techniques detailed below.	Very common equipment. Routinely operated by any material science laboratory. A few hours or days for detailed analysis of a sample.	Numerous artifacts due to sample preparation or examination are known and can be avoided by clever teams.
TEM imaging	Direct observation of the microstructure	Ibid.	Grain shape, defects (dislocations, cavities). Details of the interfaces. SPPs	The easiest way to look at a thin foil.	Rather easy to operate and interpret at standard magnifications. Only few limitations.
TEM diffraction	Crystallography of the (single and selected) grain analysed.	Ibid. with selection of the e-beam coming from only one grain.	Image one cut of the reciprocal space of the crystal analysed. By rotation of the sample, complete description. Epitaxy between grains. Discrete texture analysis. Nature of the defects; Burgers' vector of the dislocations.	Skilled operators, trained on the crystallographic systems of interest obtain this type of information easily.	Lower resolution compared to X-ray diffraction.
TEM chemistry (STEM) X-ray Scanning Transmission Microscopy	Chemistry of the atoms under the beam.	Ibid., but selection of the area to be analysed by focusing the beam.	Composition by examination of the X-ray spectrum.	Usually this technique is performed using a STEM mode. Thus it requires a specific equipment on the TEM in addition to the Energy Dispersive X-ray Spectrometer.	Not very sensitive for light elements. Small e- beam widening along its path in the foil.
TEM chemistry EELS Electron Energy Loss Spectroscopy	Chemistry of all the area under observation.	Same area of observation as for imaging. Multiple grains, synthetic view.	Fast observation of the chemistry in connection with the imaging mode. Global view of the sample. Fast measurements. Difficult below 0.1at%,	Usually this technique is performed using a STEM mode. In addition, it requires a specific equipment for the selection of the electron beam with a given energy loss.	Good sensitivity for light elements, not too much for heavy ones.

ANT International, 2011

4 Alloys and microstructure

4.1 Capture cross-section: the dominating property

Zirconium alloys have to meet many requirements to provide good service in the conditions that components experience during operation in thermal reactors that use water for heat-transport. The key property of structural materials for fission reactors is their capture cross-section for thermal neutrons; it should be as low as possible to maintain the nuclear chain reaction. The cross-section represents the probability of a reaction between the atomic nucleus of the metal and the impinging particle and has the dimensions of area. The cross-section for a single nucleus is the microscopic cross-section, σ . Since the heavy nuclei have diameters of about 10^{-14} m, then it is not surprising that σ for many elements is about 10^{-28} m². This number is often called a “barn” or b. The macroscopic cross-section, Σ , represents the cross-section of all the nuclei, N , in a standard volume, $N \text{ m}^{-3}$; it has the dimensions of a reciprocal length because $\Sigma = \sigma N \text{ m}^2 \cdot \text{m}^{-3}$. For an element:

$$\text{Eq. 4-1:} \quad \Sigma = \sigma \rho N_0 / A$$

Where

- ρ = density of the element;
- A = atomic mass;
- N_0 = Avogadro number.

For an alloy, Σ must be summed for the number of atoms of each element present.

4.2 Zirconium alloying guidelines

The main requirements for an alloy lead to the following guidelines:

- 1) Alloying elements should not substantially increase the thermal neutron absorption; this condition limits the number of alloying elements for zirconium.

Table 4-1 summarises the effect on Σ of a zirconium alloy with some elements. These cross-sections are for the addition of 1 wt% of the element using Eq. 4-1; low values are required. With low neutron capture cross-section, O, Al, Mg, Pb, Si, Sn, Nb and Y are suitable as major alloying elements for zirconium while Hf, W and Co are immediately disqualified and must be minimised. Other elements with moderate cross-sections can be added in small quantities if they impart desirable properties, for example, Fe, Ni and Cr for corrosion resistance.

- 2) An alloying element should not transmute to isotopes with high capture cross-sections or isotopes that adversely affect important properties, like corrosion resistance. An alloying element should not contain isotopes that produce long-lived radioactive species after irradiation (e.g., Co).
- 3) Alloying should maintain or minimise the degradation of corrosion resistance of the material in water and steam, and maintain or reduce its propensity for hydrogen uptake (see Section 10).
- 4) Alloying and trace elements have to maintain or increase tensile strength and retain adequate ductility and resistance to cracking at reactor operating temperatures during neutron irradiation.

Table 4-1: The influence of alloying elements on thermal neutron capture by zirconium alloys.

Element	σ_a barn	Σ with 1 wt% alloying element [$\text{cm}^2\cdot\text{cm}^{-3}$]	Element	σ_a barn	Σ with 1 wt% alloying element [$\text{cm}^2\cdot\text{cm}^{-3}$]
Zr	0.18	0.0079	Nb	1.1	0.0084
Al	0.23	0.0081	Mo	2.5	0.0094
Si	0.13	0.0079	Sn	0.6	0.008
Ti	5.8	0.014	Sb	5.5	0.092
V	5.1	0.014	Te	4.5	0.0088
Cr	2.9	0.012	Hf	105	0.032
Fe	2.53	0.011	Ta	21.3	0.014
Co	37	0.06	W	19.2	0.014
Ni	4.6	0.014	Be	0.009	0.0073
Cu	3.69	0.012	O	0.0002	0.0079
Ge	2.35	0.009	Mg	0.063	0.006
Y	1.3	0.0082	Pb	0.17	0.0071

ANT International, 2015

- 5) Maintaining deformation resistance during irradiation is important, especially for structural components that are required to have lifetimes of several decades, for example, pressure tubes. This requirement implies a stable microstructure.
- 6) The alloy must be amenable to processing and joining, including by welding.
- 7) The alloy should have a reasonable cost for mass production of components.

Requirements 1 and 2 refer to all zirconium components that operate in thermal reactor cores. Requirements 3–6 are interrelated and have to be met during fabrication, and operation of components under fast neutron irradiation at high temperatures and in aggressive environments. Requirement 7 has to be included in estimates of the unit energy costs for the lifetime of the whole reactor. Tin, niobium and iron in various combinations have emerged as the most valuable alloying elements.

4.3 Phase diagrams in zirconium alloys

Zirconium has an allotropic transformation from a low temperature, hexagonal close packed (HCP) crystal structure, the α -phase, to a high temperature body centered cubic (BCC) crystal structure, the β -phase. In pure zirconium the $\alpha \leftrightarrow \beta$ transformation takes place at 863°C (1136 K).

The systems of binary alloys with elements that might be used to alloy zirconium (O, Sn, Nb, Fe, Ni, Cr, Al, Cu, Be, Y, Mo, Gd, V, S), or may be present as impurities (C, N, S, Si, Hf, P) or might build up in alloys during operation (H from corrosion or Mo from transmutation) can be subdivided into three types:

- 1) complete solubility in the solid state (Hf),
- 2) expanded α -region, with the temperature of $\alpha \rightarrow \beta$ transformation greater than for pure zirconium. These elements are α stabilizers: O, Sn, C, N, Al, and S,

- 3) expanded β -region, with the temperature of $\alpha \rightarrow \beta$ transformation lower than for pure zirconium. These elements are β -stabilizers: Nb, Fe, Ni, Cr, Cu, Be, Y, Mo, Gd, V, Si, and H.

Solid solutions in the α -phase can also be classified into substitutional, where the Zr atoms are replaced by an alloying atom, and interstitial, when the alloying atoms fit into either octahedral or tetrahedral holes in the HCP lattice. Since nuclear considerations control the concentration of most alloy additions, and the α -phase is the preferred phase at reactor operating temperatures, the solubility limit of alloying elements in the α -phase is of most interest. Once the limit is exceeded, a second phase forms.

In the following, phase diagrams based on experiments and thermodynamic models are presented for the principal alloying elements for nuclear applications of zirconium.

4.3.1 Zr-O system

Oxygen is a notable element for the microstructure and properties of zirconium. More than hundred years were spent developing methods of producing ductile zirconium by having a low inventory of interstitial impurities, mainly oxygen. Oxygen is also beneficial and is introduced into zirconium alloys to maintain strength and creep properties without affecting corrosion resistance. Care must be taken to balance each facet since oxygen might enter zirconium during fabrication of components and during service from interacting with water to form a surface oxide coating.

Data on the Zr-O phase diagram are summarized in Figure 4-1 [Ma et al, 2008]. Oxygen raises the $\alpha \rightarrow \beta$ transformation temperature up to the zirconium melting temperature and is an α -stabilizer, expanding the α -region. The maximum oxygen solubility limit in α_{Zr} is about 35 at.% (8.63 wt%) at 2065°C and in β -Zr it is about 10.5 at.% (2.016 wt%) at about 1970°C. The oxygen in solid solution in α -zirconium is interstitial in octahedral sites. In the Zr-O system the only available stable oxide is ZrO_2 that has several phase variations. The low temperature monoclinic phase is stable up to about 1205°C; at this temperature it transforms to a tetragonal structure that converts to the cubic phase at about 1500°C.

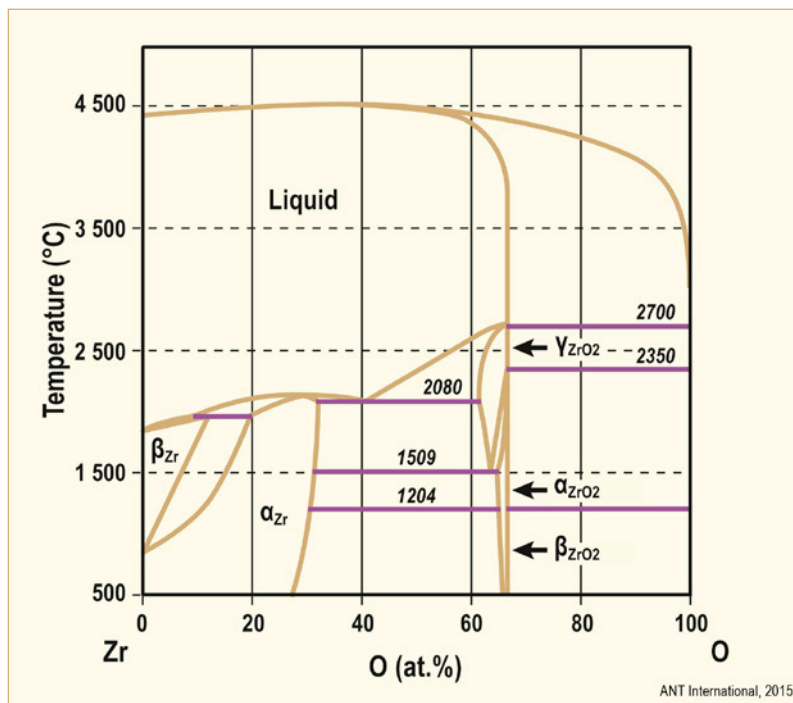


Figure 4-1: Zr-O phase diagram, after [Ma et al, 2008].

5 Fabrication Processes

5.1 First stages

The components of interest are cladding tubes, water rods, guide tubes, sheet material applied for spacers and flow channels, and pressure tubes.

The manufacturing process can be divided into three major stages.

- 1) a series of steps to produce high-purity sponge zirconium
- 2) the process steps resulting in homogeneous tube hollows with a low content of volatile impurities (ingot melting, β -forging, and β -quenching)
- 3) the process steps to secure
 - a) dimensional accuracy
 - b) the desired microstructure and texture
 - c) the strength, the ductility, and good in reactor performance (extrusion or hot rolling, and cold deformation in several steps to the final dimension with intermediate and final annealing).

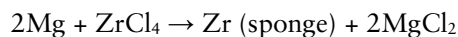
The first stage is the production of high-purity reactor-grade zirconium sponge. It starts from zirconium sand, Zr-Hf SiO₄ (with 1-3% Hf). The silica fraction is removed by one of three processes: carbochlorination at ATI Wah Chang (WC) and Western Zirconium in USA and Cezus (CZ) in France, fluorosilicate fusion at the Chepetsky Mechanical Plant (ChMP) in Russia, and alkali fusion at the Nuclear Fuel Complex (NFC) in India.

Hf has a very large thermal neutron cross section and has to be separated from Zr during the manufacturing. Four processes are available: fractional crystallization is used at ChMP, solvent extraction by either methyl isobutyl ketone-thiocyanate (MIBK) at WC or tributyl phosphate (TBP)-nitric acid at NFC, and extractive distillation at CZ.

The chemical impurity has to be limited. There are three different processes to produce Zr metal:

- the Kroll process,
- the electrolytic process,
- and the Van Arkel process.

In the Kroll process the metal oxide from the separation process is chlorinated to zirconium tetrachloride then reduced to sponge Zr by magnesium:



This process is the main commercial method for producing Zr metal at WC, CZ and NFC. At ChMP, Zr powder is produced at the cathode during electrolysis of potassium hexafluorozirconate:



This ChMP process is being phased out and replaced by the Kroll process.

Very pure Zr is produced by the iodide transport or Van Arkel process. It is not used in most commercial applications.

In the second stage the sponge is mixed with high purity alloying elements together with refined return scrap and pressed into briquettes, which are welded into a 3-5 m long cylindrically shaped ingot. The ingot melting process is outlined in Figure 5-1. The consumable electrode is arc melted into a cylindrical water cooled copper mold slightly larger than the electrode. A high vacuum is necessary during melting to prevent O and N absorption. The molten pool is about 1 m deep. The melted metal freezes against the cold Cu mold, and forms solid layers of the Zr alloy. The first ingot is cut into pieces and re-welded for a new ingot. To achieve uniform chemical composition, the arc melting is repeated 2-4 times. Furthermore, the concentration of volatile impurities decreases significantly with the number of remeltings; for example, chlorine concentration is reduced by a factor of about 800 by melting four times (Figure 5-2). Up to the late 1990s Zr alloys were normally melted 2 times, since then 3-4 times. Melting represents the last chance to change the composition of the alloy, apart from pick-up of O and H during forming and heat-treatment at elevated temperatures.

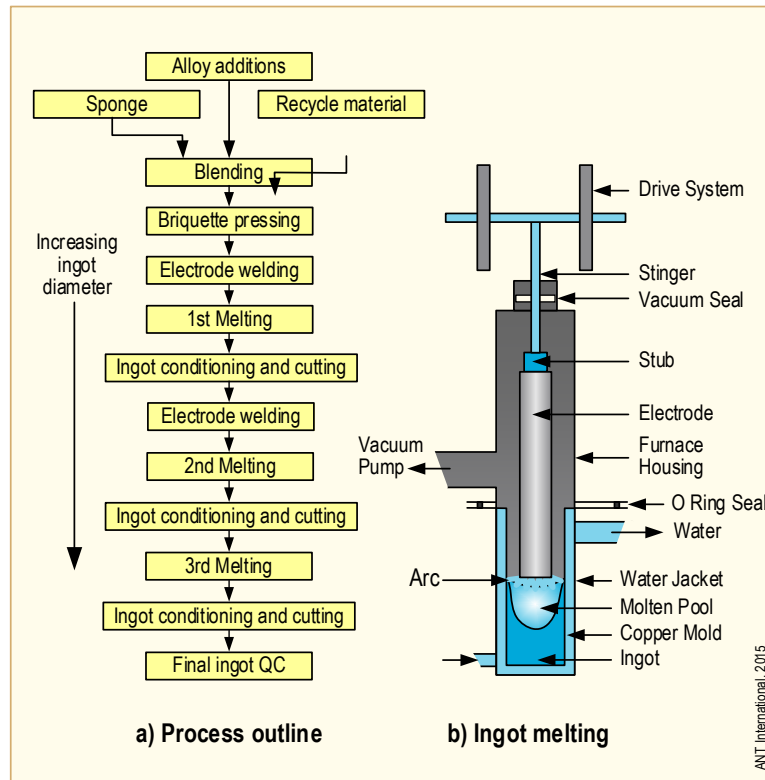


Figure 5-1: Outline of the Ingot Melting Process for Zirconium alloys.

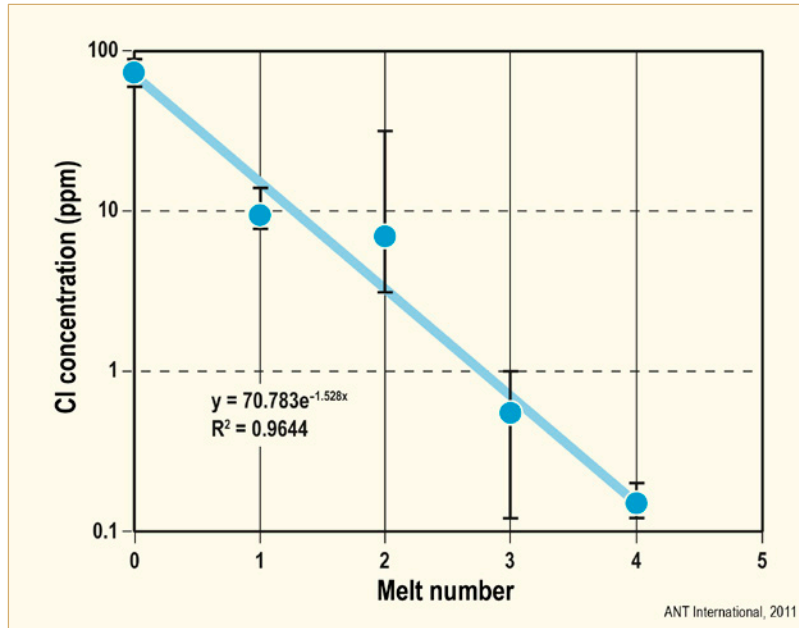


Figure 5-2: Reduction of volatile Cl with the number of remeltings, after [Theaker et al, 1994].

5.2 Mostly α -alloys

The next step is forging of the ingot, which proceeds after machining and heating to about 1040°C for 4-12h, using a forging press, rotary forge or rolling mill in several steps. In alloys based on the α -phase, for example, Zircaloy, deformation in the $\alpha+\beta$ range is minimized to prevent a non-uniform distribution of SPPs. Absorption of O and N from air limits the time at temperature. Afterwards, the β -quenching step, is performed after preheating to about 1050°C for 0.4-1.5h, a <45-90 sec transfer time, and by dropping into a water bath. The decomposition of β -phase to α -phase and intermetallics leads to a Widmanstätten structure, which could be either a basketweave structure (BW) or a parallel plate structure (PP), as shown in Figure 5-3. Impurities (such as Cl, Si, C, and P.) can promote a basketweave structure, which is the preferred microstructure for good mechanical properties.

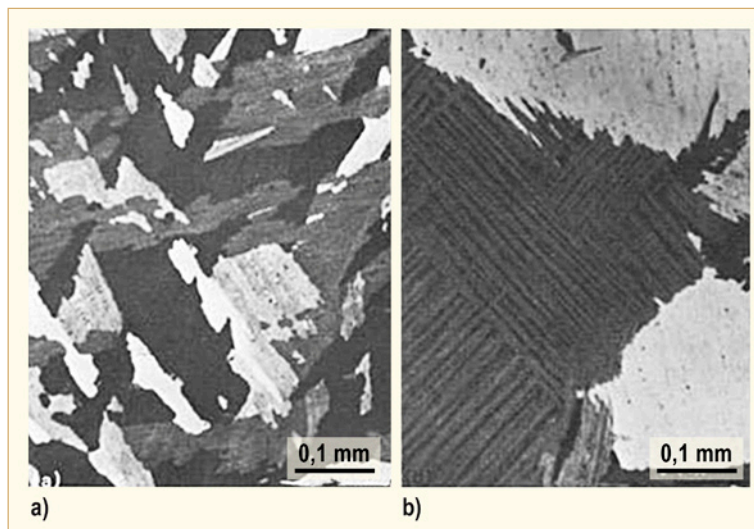


Figure 5-3: Microstructure of Zircaloy-4 cooled from the β phase field (4h at 1100°C, air cooled) demonstrating the two different Widmanstätten morphologies (a) Basketweave structure, Material A, (b) Parallel plate structure, Material B, [Holt, 1970].

6 Slip and twinning systems during plastic deformation

6.1 Unirradiated material

In hexagonal close packed (hcp) α -Zr the plastic deformation modes are

- slip systems, which are limited to deformations in the important $\langle a \rangle$ direction to at least at $<500^\circ\text{C}$ and
- twinning

The result is formation of a strong deformation texture. The different microstructures after deformation by slip and twinning are shown in Figure 6-1.

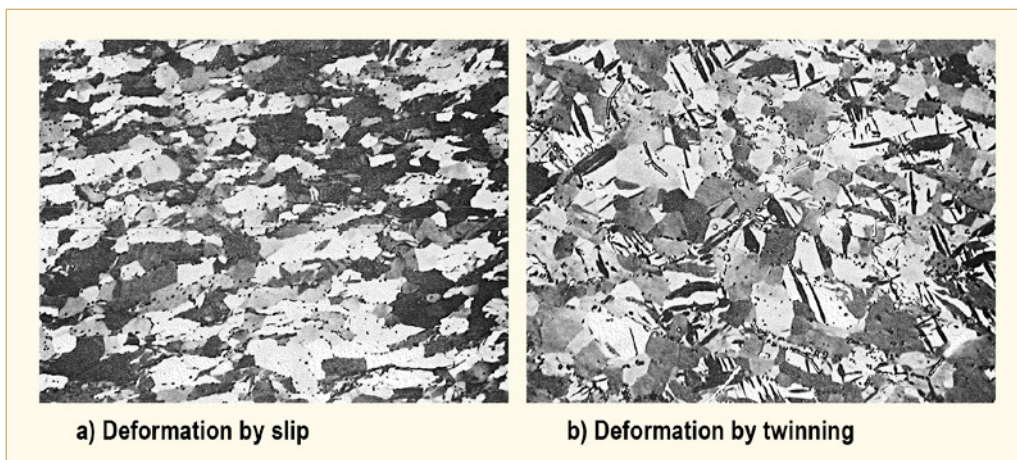


Figure 6-1: Metallographic structure of the highly deformed regions of Zircaloy-2 tensile specimens [Cheadle, 1975]. Magnification about 250X

In the α -structure of Zr at room temperature and up to about 400°C usually prism $\langle a \rangle$ slip occurs on the $\{10\bar{1}0\}$ planes in the $\langle 11\bar{2}0 \rangle$ directions (Figure 6-2a) and basal $\langle a \rangle$ slip on the $\{0001\}$ planes in the $\langle 11\bar{2}0 \rangle$ directions (Figure 6-2b). Furthermore, in regions of high stress concentration, such as grain boundaries, $\langle a \rangle$ slip can occur on the $\{10\bar{1}1\}$ planes. A slip system with a component in the $\langle c \rangle$ direction has been observed only under constraint and at high deformation temperatures. The corresponding $\langle c + a \rangle$ slip mode is slip that occurs on first and second-order pyramidal planes $\{10\bar{1}1\}$ and $\{11\bar{2}1\}$ in the $\langle 11\bar{2}3 \rangle$ direction (Figure 6-2c).

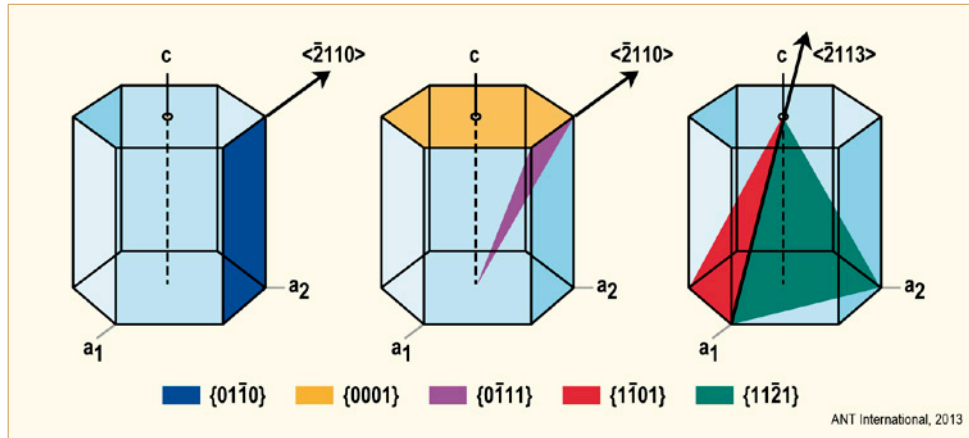


Figure 6-2: Schematic illustration of slip systems in HCP: (a) basal slip; (b) prismatic slip; and (c) pyramidal slip, after [Tenckhoff 1988].

Another important deformation mode, is twinning. Twinning results when a portion of the crystal takes up an orientation (by small movements of atoms, less movement than in slip process) that is related to the orientation of the rest of the lattice in a symmetrical way. The twinned portion of the crystal is a mirror image (i. e., twin) of the parent crystal. This deformation is shown schematically in Figure 6-3. Twinning proceeds in α -Zr on pyramidal planes of different orders and modes, and results in deformations with $\langle c \rangle$ components. Under tension, twinning proceeds along the $\langle 0001 \rangle$ direction on the $\{10\bar{1}2\}$ and $\{11\bar{2}1\}$ planes and under compression on the $\{11\bar{2}2\}$ planes (Figure 6-4).

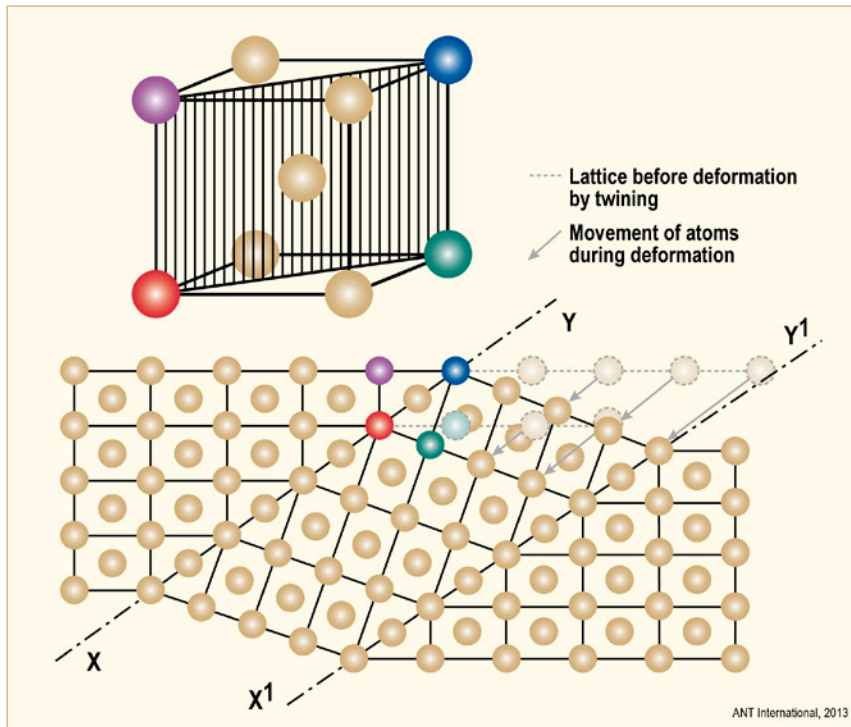


Figure 6-3: Schematic representation of twinning. The twinning planes are along XY and X^1Y^1 , and the region between them is the twin, after [Keyser, 1952].

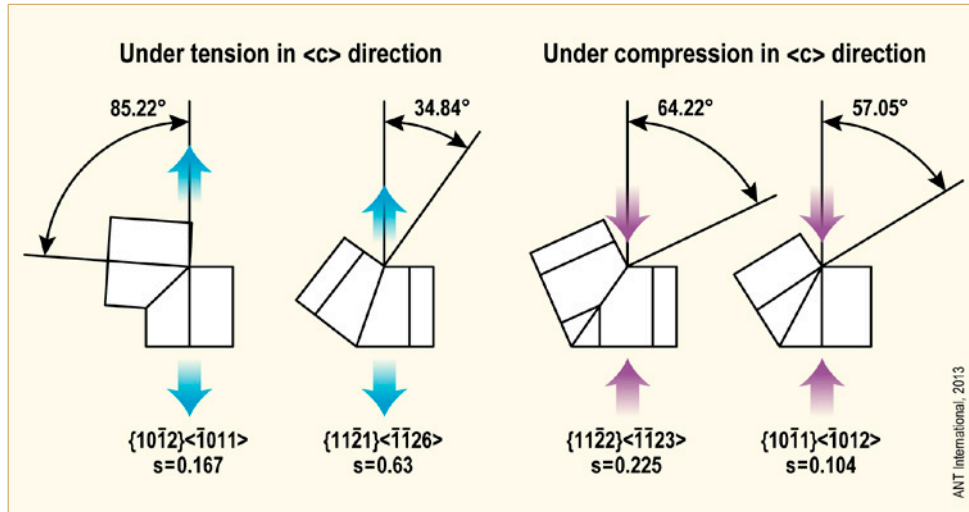


Figure 6-4: Twinning systems in alpha zirconium, after [Tenckhoff, 2005].

To predict whether slip or twinning will proceed, the Schmid factor, which is a purely geometrical relationship between the corresponding deformation mode and the direction of force (Figure 6-5a), must be taken into account. The resolved shear stress on the slip/twinning plane (τ) is given by the following equation

$$\tau = \frac{F}{A} \times \cos(\varphi) \times \cos(\lambda)$$

where F = the externally applied force in the direction of the rod axis, A = cross section of the crystal, φ = angle between the normal to the slip plane and the direction of force of the external reference system, and λ = angle between the slip direction and net force of the external reference system. The product “ $\cos(\varphi) \times \cos(\lambda)$ ” is the Schmid factor. Figure 6-5b shows how the Schmid factors for prism slip and twinning depend on the intermediate stress angle.

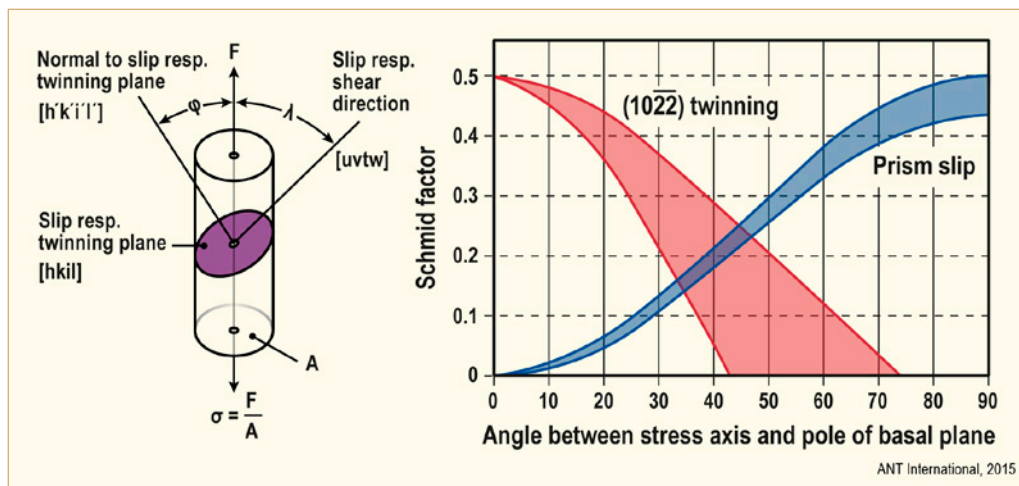


Figure 6-5: (a) Relationship between the shearing stress acting in the deformation system and the externally applied force on a single-crystal, (b) Schmid factor for prismatic slip and (1022) twinning as function of the angle between stress axis and pole of basal plane, after [Cheadle, 1975].

7 Texture and Anisotropy

Anisotropy in Zr-alloys has two sources:

- 1) Mechanical anisotropy resulting from deformation modes (slip and twinning) in the alloy. This anisotropy can change during service due to, for example, metallurgical condition, temperature and irradiation, all of which can influence the nature of the active deformation processes.
- 2) Crystallographic anisotropy (texture) resulting from specific arrangement of atomic planes in the alloy. This anisotropy is fixed by heat treatment and fabrication routes, and changes only locally during service. Irradiation itself does not change this anisotropy.

7.1 Texture

At temperatures below about 825°C zirconium alloys have the hexagonal-close-packed (hcp) structure. Important planes in that structure are shown in Figure 7-1 [Tenckhoff, 2005]: basal plane, prism plane and pyramidal plane. The unit cell is marked by the heavy lines in Figure 7-1.

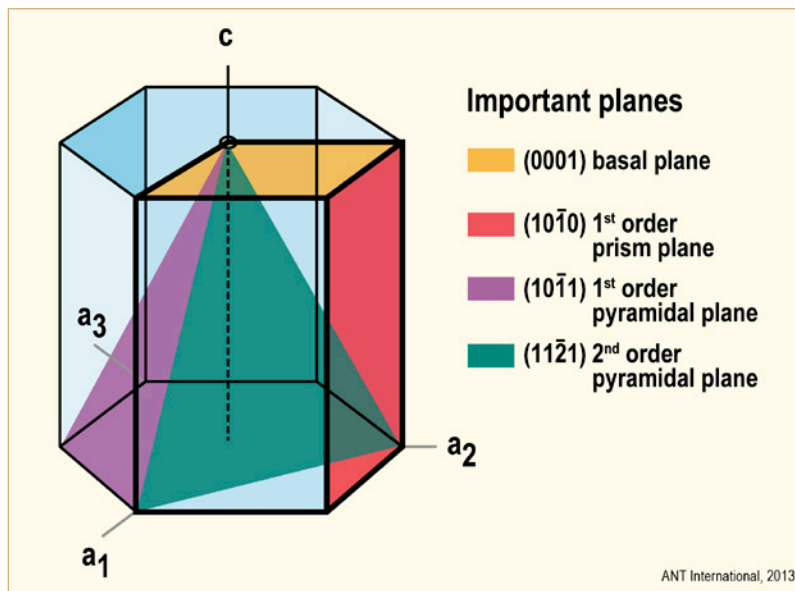


Figure 7-1: Crystallographic characterizations of the hcp elementary cell, after [Tenckhoff, 2005].

In the hexagonal close-packed crystal structure, as for zirconium alloys, the Miller-Bravais system is used to identify planes and directions. The indices are based on four axes: the three axes a_1 , a_2 , a_3 , are 120° apart in the basal plane, and the vertical c axis is normal to the basal plane, as shown in Figure 7-1, and the indices are given as $(hkil)$. For clarity, $(hkil)$ indicates a specific plane, while $\{hkil\}$ indicates a family of planes, identical in geometry relative to the lattice, but identified specifically depending on the choice of axis origin. For instance $(10\bar{1}0)$, $(0\bar{1}\bar{1}0)$ and $(\bar{1}\bar{1}00)$ are all prism planes of the $\{10\bar{1}0\}$ family. The indices indicate the reciprocal of intercept of the plane on the four crystal axes. Example: a $(10\bar{1}0)$ plane intercepts the a_1 axis at 1 unit, the a_2 axis at infinity (∞), the a_3 axis at -1 unit, and the c axis at infinity. It is noted that $i = -(h+k)$. The index l indicates the reciprocal of where the plane of interest intercepts the c -axis. For prism planes this is at ∞ , so $l = \frac{1}{\infty} = 0$ indicates the plane is perpendicular to the basal plane, and when $l \neq 0$, the plane is inclined at some angle to the basal plane. The basal plane itself is therefore designated as (0001) , but could be (0002) , and pyramidal planes (see Figure 7-1) are $\{10\bar{1}1\}$ and $\{11\bar{2}1\}$.

Directions in the HCP system are given as $[hkil]$, but reciprocals are not used for directions. Families of directions are given as $\langle hkil \rangle$. Often directions are given in terms of the a or c axes, so that “ $\langle c \rangle$ component” or “ \bar{c} -component” dislocations have Burgers vectors with a strong component in the c-direction $[0001]$ in it. Similar terminology applies to $\langle a \rangle$ component or \bar{a} -component dislocations.

Texture is commonly described by pole figures obtained by X-ray diffraction, by Kearns f -parameter numbers calculated from pole figures, and, less commonly, by a mechanical measure of contractile strain ratio. Figure 7-2 gives a direct pole figure for a typical fuel cladding tube. What is shown is a 2-dimensional (stereographic) projection of a 3-dimensional (spherical) distribution of the normals to the basal planes (pole) of a large number of grains in the cladding. (Note: if the average grain size is greater than about $40 \mu\text{m}$ (ASTM 36) the measurements become unreliable [Lewis et al, 1982].) The pole figure is defined by three directions in the tubing: LD (axial), TD (circumferential) and ND (radial or through-thickness). The numbered contours give the times-random intensity of the basal pole in the given direction. In this specific case the value is higher along the TD direction (value 6-7) than in the LD direction. In stereographic projections there is a 90° angle between the ND and TD or LD directions, and for Figure 7-2 the maximum intensity of basal plane poles is about 30° from the radial direction in the tube. This is seen more easily in Figure 7-3 where the basal pole intensity in the TD-ND plane is plotted as a function of angle.

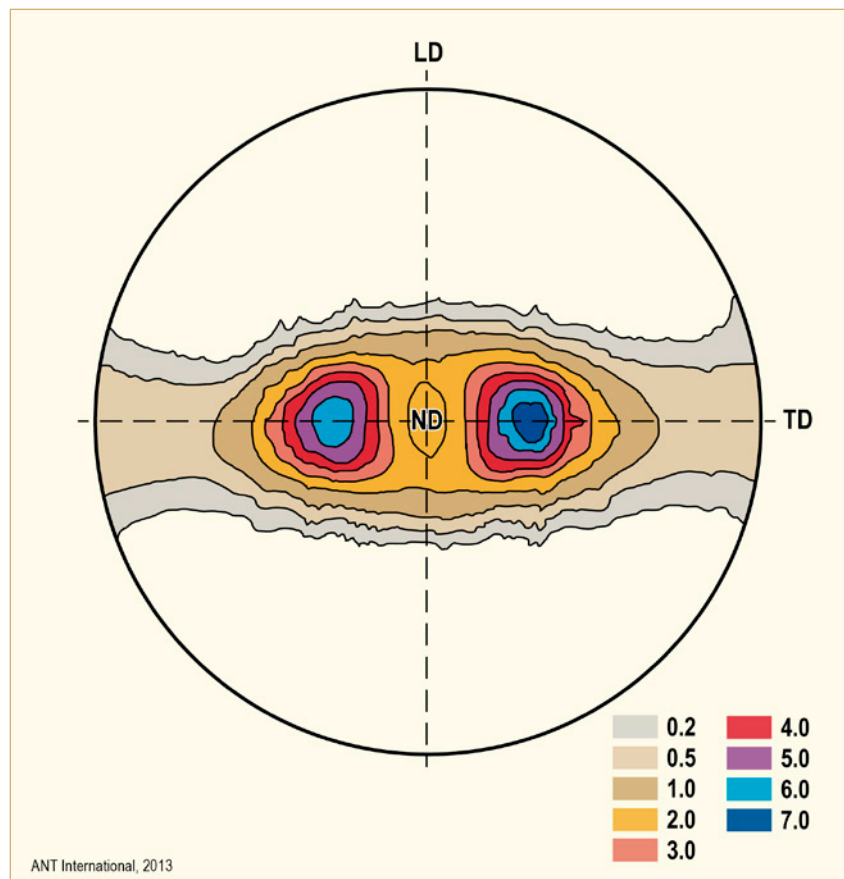


Figure 7-2: Typical texture of cold worked Zircaloy cladding tube, (0002) direct pole figure, after [Lewis et al, 1982].

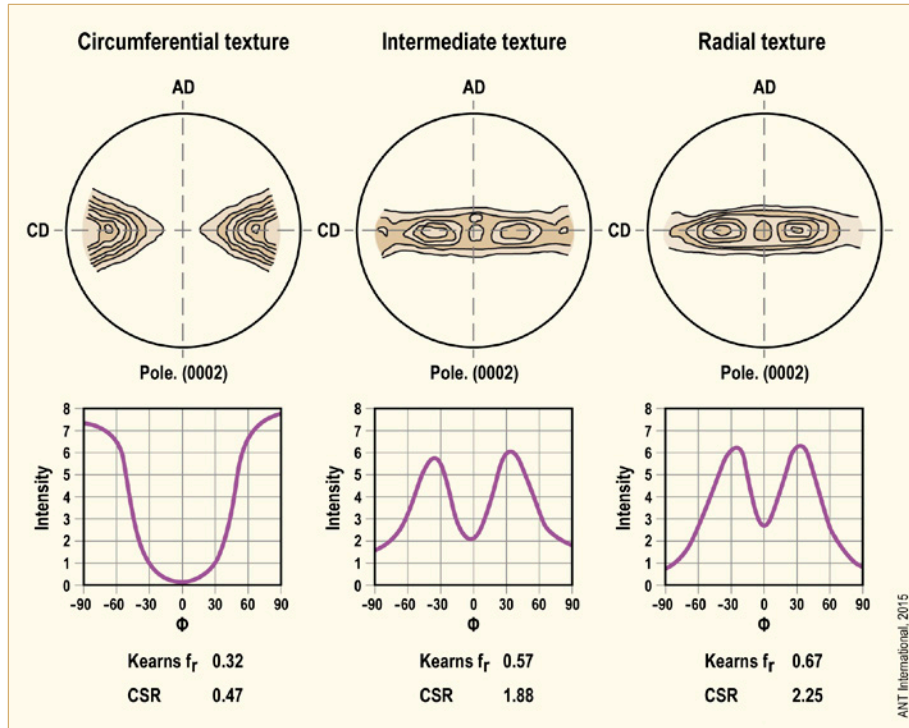


Figure 7-3: Crystal texture represented by (0002) pole figure, intensity plot, Kearns texture parameter and contractile strain ratio (CSR), after [Schemel, 1989].

To obtain a more complete description, pole figures of other planes are generally obtained. Figure 7-4 gives the companion $(10\bar{1}0)$ prism pole distribution for the Figure 7-2 tube. It is seen for this ~70% cold-worked tube the prism poles are strongly aligned in the LD direction. This orientation is common for cold-worked tubing, whereas for recrystallized tubing they are rotated about 30° from the LD direction.

8 Deformation

8.1 Types of deformation during fabrication

As discussed in Section 5, fabrication of cladding or pressure tubes or “flat” components such as grids, spacers, channels etc., requires combinations of cold, warm and hot work (deformation) processes. The three processes are classified according to the relative ease of deformation (strength and ductility) and residual effect on microstructure. Strength and ductility are primarily affected by the ease by which dislocations move through the zirconium lattice, which in turn is affected primarily by dislocation density, grain boundary density (grain size) and temperature.

8.1.1 Cold work

Cold work occurs in the temperature range in which no recrystallization occurs. Theoretically, this means below about 400°C (673K), but in practice “cold working” refers to “room temperature” (about 25°C [298K]) or in the extreme, below 100°C (373K). At these temperatures, dislocation density increases rapidly from about $1 \times 10^{10} \text{ cm}^{-2}$ in the fully recrystallized (RXA) condition to about $10 \times 10^{10} \text{ cm}^{-2}$ at 70% cold work (70% reduction in area). For normal rolling or pilger processes, 70-80% cold work is the maximum before loss of ductility results in cracking. Typical microstructures observed using light microscopy are given in Figure 8-1, where the effect of annealing after 20% cold work is shown, and Figure 8-2, where RXA and SRA structures are shown.

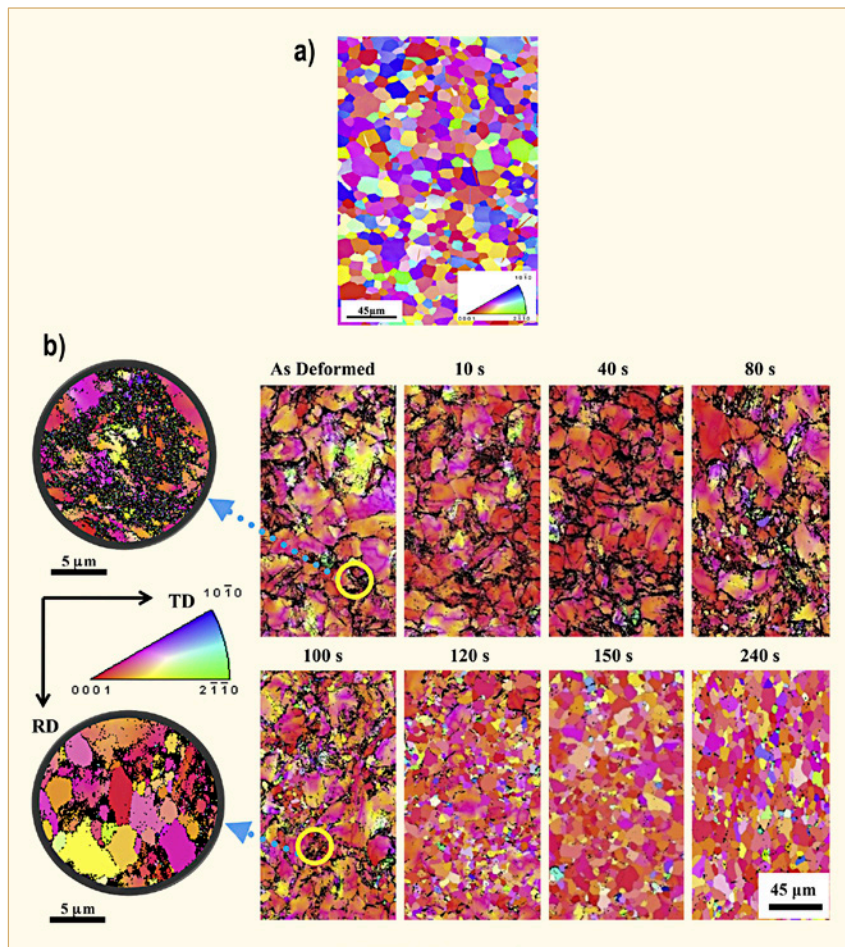


Figure 8-1: Microstructure of a) fully recrystallized Zircaloy-4 and b) 20% cold worked Zircaloy-4, followed by annealing at 650°C (923K) for various times [Kumar et al, 2015].

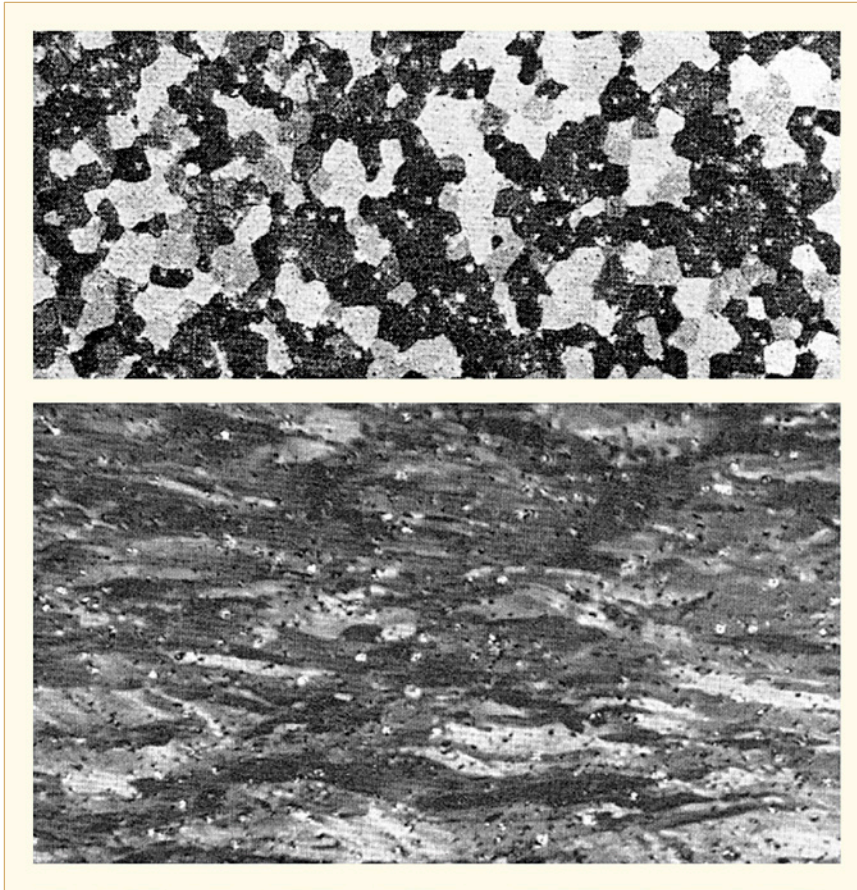


Figure 8-2: Micrograph of typical above) RXA tubing showing equiaxed grains and uniformly distributed second phase particles (SPPs) and below) SRA showing distorted grains after 70% coldwork. Zircaloy-4, polarized light, about 1000X, [Schemel, 1989].

Referring to Section 5, cold working processes are used for tube reduction pilgering, and for final steps for flat products. If 70-80% cold work (reduction of area) is required then a recrystallization anneal is required between deformation steps, usually conducted at 500-700°C (773-973K).

Cold working by either pilgering (where both the tube diameter and wall thickness is reduced) or by rolling (where primarily the plate thickness is reduced) is crucial for development of texture and grain size and shape of the final products.

8.1.2 Warm work

Warm working occurs in a temperature range in which recrystallization may or may not occur, but lower than for any phase change. For Zircaloys, it is below about 800°C (1073K) and for Zr-Nb alloys below about 600°C (873K). In practice, warm working is in the lower range. For instance, for bending flat strip in “L” shape for BWR channels, the temperature is around 150°C (423K). Because the temperature is higher than for cold working, the ductility is also higher, allowing local deformation >70%.

8.1.3 Hot work

Hot working occurs at high temperatures where large reductions in area are required, and where the residual hot working microstructure will be altered later by additional working and heat treatment. Temperatures are such that continuous recrystallization occurs, sometimes at temperatures above phase change boundaries. Again referring to Section 5, at the ingot stage, hot pressing or rotary forging often begins in the beta phase (usually not higher than 1100°C (1373K)) and continues during self-cooling to the lower alpha plus beta ($\alpha+\beta$) phase, greater than 815°C (1088K). At the billet stage, extrusion is conducted at about 650°C (923K) for Zircalloys and about 815°C (1088K) for Zr2.5Nb. Microstructures for extrusion (at an unusually high temperature) are shown in Figure 8-3. A uniformly distributed microstructure is desired at this stage, to be followed by cold pilgering for Zircaloy and Zr1Nb tubing, and cold drawing for Zr2.5Nb pressure tubes.

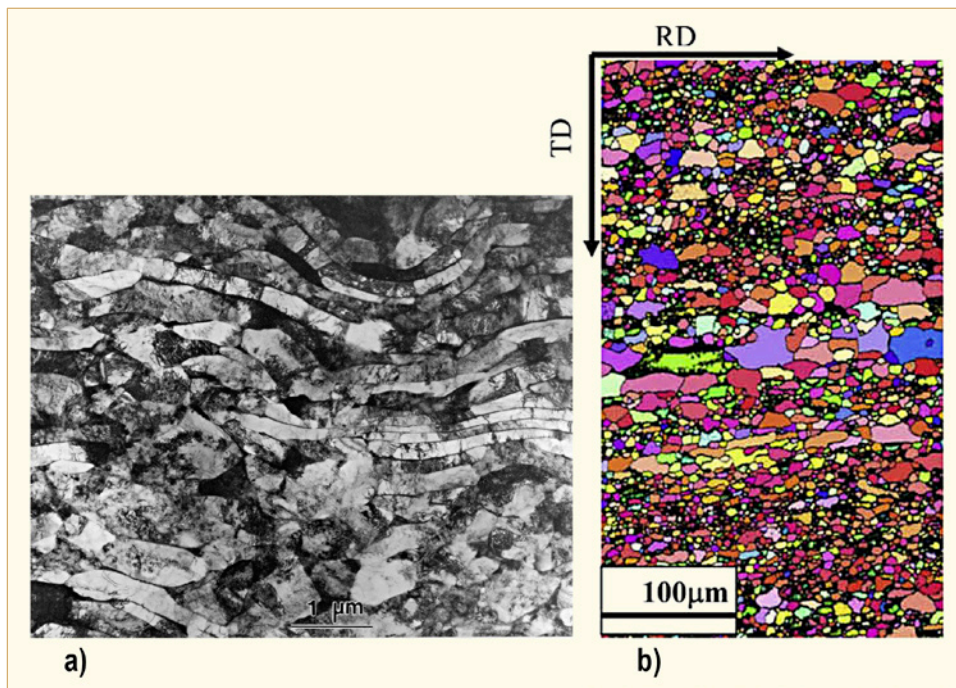


Figure 8-3: a) Transmission electron micrograph of Zr-2.5Nb pressure tube. The vertical direction is the radial direction and the horizontal direction is the circumferential direction. The larger grains are α -phase and the dark phase surrounding them is β -phase, [Micrograph from O. T. Woo (CNL)]. b) Microstructures revealed by EBSD (electron backscattered diffraction) images of a hot extruded (825°C (1098K)) Zircaloy-4 tube. RD and TD correspond respectively to axial and circumferential directions of the tube, [Mani Krishna et al, 2008].

9 Second phase particle (SPP)

9.1 Kind, size and distribution of SPPs

The type, size, and distribution of second phase particles (SPPs) formed in zirconium alloys depend on alloying composition, on the cooling rate from the β -temperature phase where almost all SPP are dissolved (β -quenching step) and on the accumulated thermal inputs (annealing treatments) during the later fabrication process in the α -range (hot forging, extrusion and annealing steps after the different pilgering steps). The effect of accumulated annealing is often described by an accumulated A-parameter, a log A-parameter, or a PGP value [Adamson et al, 2002].

At temperatures in the β - or $\beta+\alpha$ - range only certain impurities, such as Cl, Si, C, P can precipitate in form of stringers or SPPs, such as ZrC and Zr₃(SiP), as described in Section 5. The solubility of all alloying elements used or considered for Zr alloys fuel rod claddings is rather high in the β -temperature range ($>\approx 960^\circ\text{C}$); however, the solubility in the α -range ($<600\text{-}800^\circ\text{C}$) is much smaller. The solubility the transition metals (TM) Fe, Cr, Ni, V, Cu (≤ 100 ppm) in the α -range ($<\approx 800^\circ\text{C}$) is very small, as described in Section 4. In contrast to the TM, several other alloying elements have a moderate solubility in the α -range, e.g. Nb ($\leq 0.3\text{-}0.5\%$), or even a significant solubility, i.e. Sn ($\leq 2\%$).

Thus, intermetallic SPPs are formed in the α -range by Fe, Cr, Ni, V, and Cu (transition metals, TM) such as ZrCr₂, Zr(FeCr)₂, Zr(FeV)₂ (hexagonal, Laves phase with lattice parameters $a\approx 0.5$, $c\approx 0.83$), respectively, Zr₂(FeNi) (tetragonal with lattice parameters $a\approx 0.65$, $c\approx 0.55$) or Zr₂Fe (orthorhombic with lattice parameters $a\approx 0.33$, $b\approx 1.1$, $c\approx 0.88$), respectively, Zr₃Fe (cubic with lattice parameters $a\approx 0.68$, $c\approx 0.53$). In the $\alpha+\beta$ -range most of the TM concentrates in the remaining β -phase if cooling rate through the $\alpha+\beta$ -range is low ($<50\text{-}500$ K/s). Figure 9-1 gives data on the amount of beta phase formed during quenching.

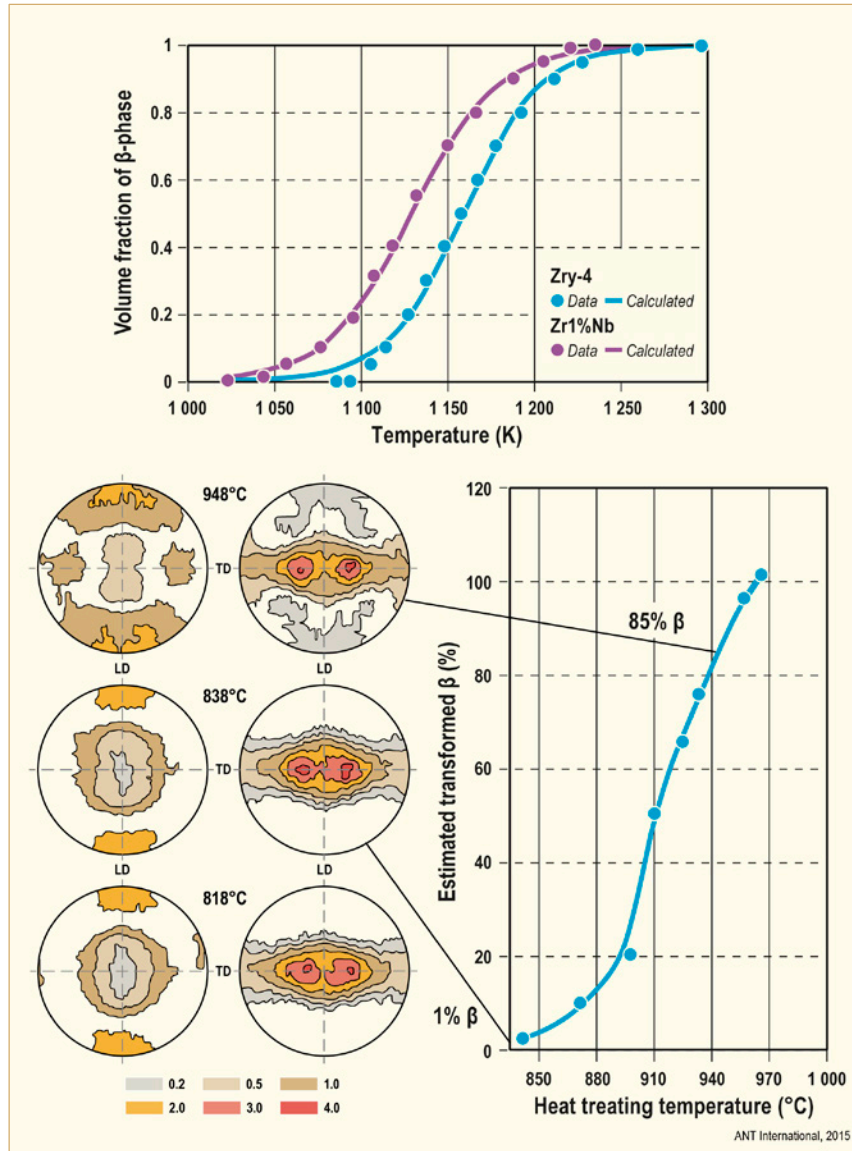


Figure 9-1: Amount of beta phase formed during quenching, top after [Forgeron et al, 2000], bottom after [Adamson et al, 2010].

In case of Zr alloys containing Fe, Cr/V, and Ni (Zircaloy type alloys) the hexagonal $Zr(FeCr/V)_2$, and the tetragonal $Zr_2(FeNi)$ are formed if the Fe/Cr ratio $<2-4$. At a Fe/Cr alloying ratio of $>2-4$, Zr_2Fe and at still higher Fe/Cr ratios, Zr_3Fe is formed in addition [Charquet, 1994]. $Zr_2(FeNi)$ is in the literature often called Zintl-phase, which is, however, not strictly correct, because the covalent bonding described for Zintl applies specifically to the alkaline metals. For more details see [Barb eris et al, 2005] and [Motta et al, 2002]. As [Garzarolli et al, 1996b] pointed out, in ZrSnFeCr-alloys with a Fe/Cr ratio <4 almost all SPP are of the $Zr(Fe,Cr)_2$ -type. If the ratio Fe/Cr is >4 under a process with a medium cooling rate through the $\alpha+\beta$ range (50K/s) or >2 under a process with slow cooling rate (1K/s), Zr_2Fe and Zr_3Fe are formed besides the Laves phase $Zr(Fe,Cr)_2$ [Charquet, 1994]. Rapid cooling from β phase favours the formation of Fe-rich zones, which will decompose into Fe-rich precipitates after thermomechanical treatment. This local enrichment is due to the preferential partition of Fe to the residual β phase on crossing through the $\alpha+\beta$ field, since Fe diffuses more rapidly than Cr. These local Fe and Cr variations are probably a major reason for the observation that the composition of $Zr(FeCr)_2$ phase varies widely from one particle to another. In a case, where the mean Fe/Cr ratio was 3.1, the minimum and maximum values were found to be 2.8 and 3.6 respectively [Charquet, 1994].

Zr_3Fe SPP exhibit only a very small solubility for Cr. Thus even at a Fe/Cr-ratio of 10, $Zr(FeCr)_2$ can be observed besides Zr_3Fe . Sometimes, another type of Fe-containing precipitates with no or only little Cr can be seen in addition to the $Zr(FeCr)_2$ -SPP if Fe/Cr <4. These precipitates often also contain some Si or/and Ni. It is assumed that these particles precipitate during β -quenching in the lower $\alpha+\beta$ -range and are stabilized by Si and Ni to form $Zr_2(FeNi)$ or $Zr_2(FeSi)$. The tetragonal $Zr_2(FeSi)$ is observed at Si contents above 50 to 80 ppm and is generally very fine. The impurity Si is sometimes added to Zircaloy-4 at low concentrations (50-120 ppm) for optimization corrosion resistance, probably via the effect of Si on the SPP distribution.

In Cu containing Zr alloys with $\leq 0.05\%$ Cu, the Cu becomes included in other SPPs, such as $Zr(FeCrCu)_2$, containing up to 5at% [Kim et al, 2008]. A Cu addition of 0.1-0.5% to Zircaloy-4 results in the formation of the tetragonal Zr_2Cu SPPs in addition to the hex. $Zr(FeCrCu)_2$ SPPs [Hong et al, 2000].

In Nb containing Zr alloys with $>0.5\%$ Nb in the $\alpha+\beta$ -range (600-900°C), the Nb content is concentrated in the β -Zr (up to 20%Nb) together with almost all Fe, Cr, V, Cu etc. if the coolant rate is not very high. In the α -range ($<600^\circ\text{C}$) above Nb solubility (>0.3 - 0.5%) the main phases are fine β -Nb (containing about 10%Zr), the fine hexagonal $Zr(NbCrFe)_2$, and the rather large cubic or orthorhombic $(ZrNb)_{2-3}(FeCr)$ SPP, depending on the Fe/Nb ratio (Figure 9-2). The hcp $Zr(NbCrFe)_2$ SPP that forms at moderate Fe/Nb ratio has a composition of about 25-35Zr-45-35Nb-30Fe % at, depending on the Fe and Nb content of the alloy) and lattice parameters $a=0.54$ nm and $c=0.87$ nm e.g. [Shishov et al, 2002] and [Shishov et al, 2007]. Some uncertainty exists on the rather large $(ZrNb)_{2-3}(FeCr)$ SPP that form at a high Fe/Nb ratio and have according [Shishov et al, 2007] a fcc crystal structure ($a=1.21$ nm) and a composition of about 60Zr-10Nb-30Fe (%at). According [Griffiths et al, 1996] and [Nikulina et al, 1996] these SPP have the composition $(ZrNb)_3(FeCr)$ and are orthorhombic with a lattice with $a=0.88$ nm and $b=0.33$ nm, according [Barb ris et al, 2004] and [Toffolon et al, 2006] this phase is a cubic $(ZrNb)_4Fe_2$ with a lattice parameter of 1.2 nm. The results and descriptions of the chemistry and crystal structure of these precipitates are controversial.

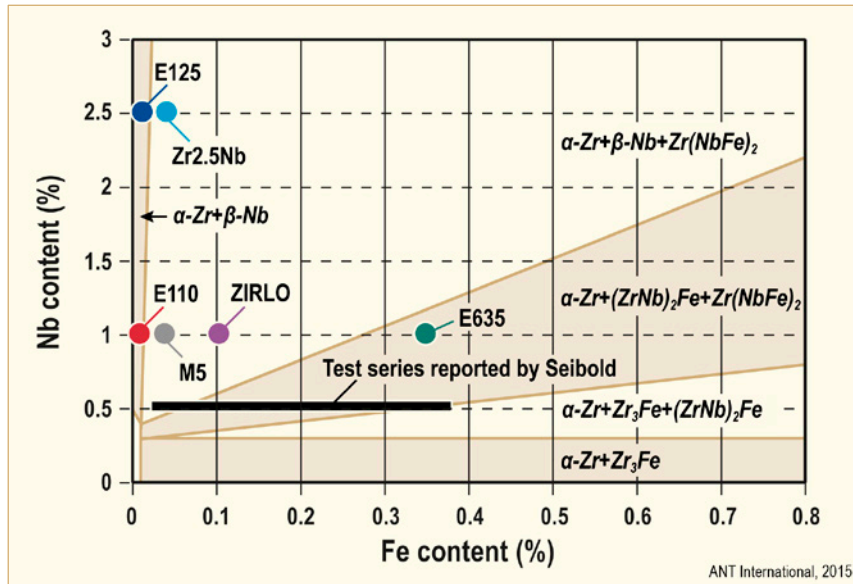


Figure 9-2: Zr-Nb-Fe ternary alloy phase diagram at 580°C, composed from information in [Toffolon et al, 2002] and [Shishov et al, 2005] modified from [Nikulina et al, 2006]. Composition given in weight%.

In Zr-Nb alloys a metastable hexagonal ω -phase can form either by quenching or by aging the Nb containing β -phase ($\beta\text{-Zr} \rightarrow \omega + \beta\text{-ZrNb-enr}$). The ω -phase formed by aging at 400°C is in the form of platelets about 25 nm square. In Zr-Nb alloys the β must contain about 7 wt% Nb before quenched ω can be formed. The ω -phase transforms finally to $\alpha\text{-Zr} + \beta\text{-Nb}$.

10 Hydrides and their effect on properties

10.1 Hydride phases and solubility limits

Zirconium hydrides are brittle and their presence represents a threat to the structural integrity of components made from zirconium alloys. The format and distribution of hydrides can have a wide variation but in their most damaging form they appear by light metallography as platelets after slow cooling, Figure 10-1 [Billone et al, 2013]. When observed by TEM, small hydrides are often precipitated in close association with one another to produce stacks of hydrides, forming a composite structure that could appear as a long stringer by light microscopy. Hydrides may precipitate in grain boundaries or α/β -boundaries. Rapid cooling to room temperature from an elevated temperature, where all the hydrogen is in solution, cannot retain the hydrogen in solution and hydrides precipitate as small needles at random and often on dislocations [Westlake, 1965]. To evaluate whether hydrides are present at operating temperatures one needs to know the concentration of hydrogen and the solubility limit of hydrogen in the material. The latter is gained from knowledge of the phase diagram of the zirconium-hydrogen system. The phase diagram is of the eutectoid type, Figure 10-2 [Zuzek et al, 1990], [Dupin et al, 1999], with the following phases: a random interstitial but terminal solid solution (TSS) in the α -phase, with a maximum hydrogen solubility, 5.93 at.% (690 ppm), at the eutectoid temperature, 550°C; the eutectoid is at a hydrogen concentration of 37.5 at.% (6535 ppm). In the β -phase, a random interstitial but terminal solid solution extends to a maximum solubility of 51.5 at.% (11 500 ppm) at 870°C. Hydrides form when the terminal solid solubility is exceeded.

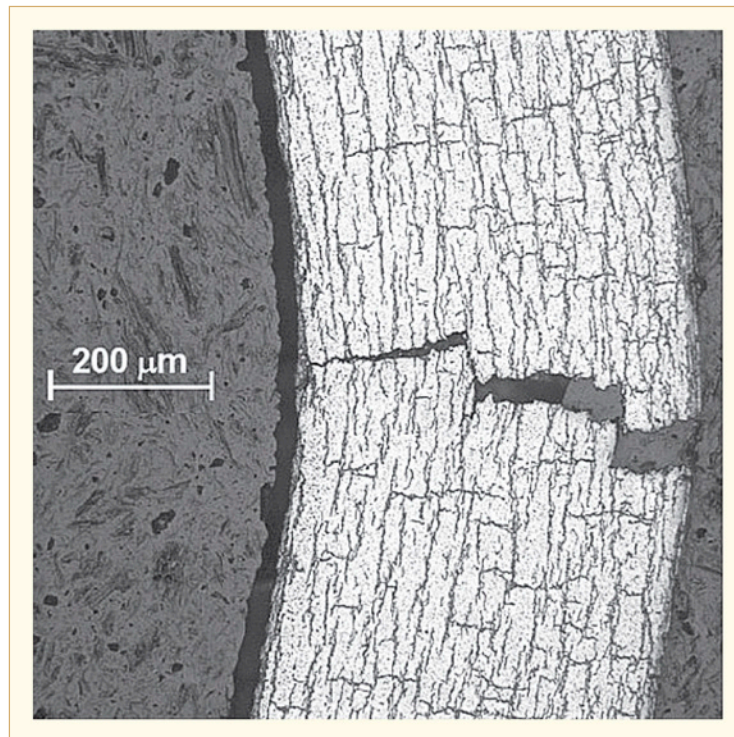


Figure 10-1: Distribution of hydride platelets on a transverse-radial plane in ZIRLO fuel cladding containing 630 ppm hydrogen cooled from 400°C with hoop stress of 190 MPa [Billone et al, 2013]

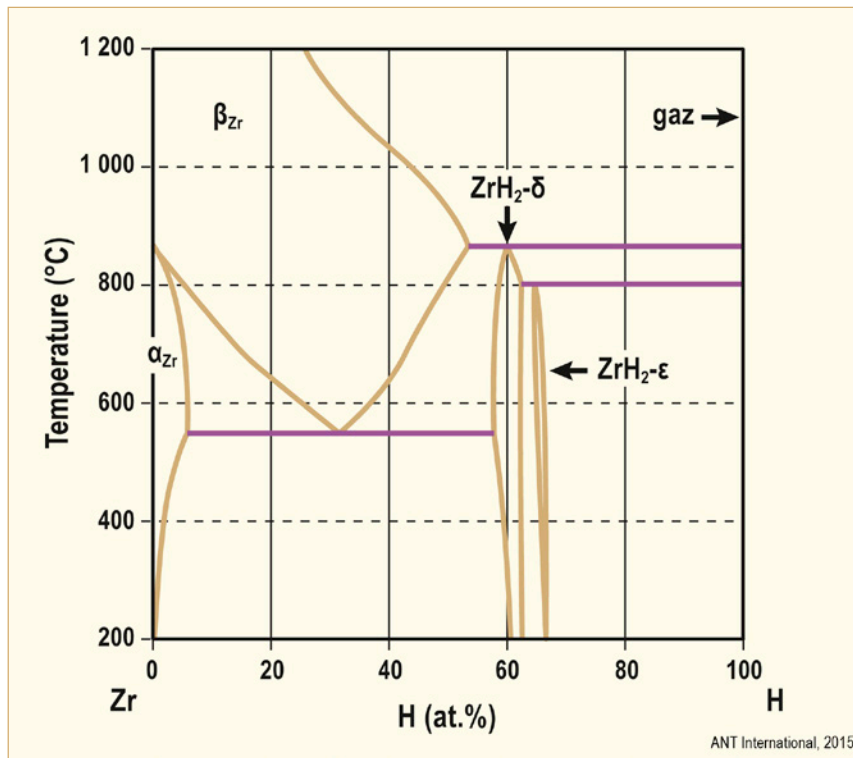


Figure 10-2: Zr-H phase diagram, after [Dupin et al, 1999]

Four hydrides have been identified called γ , δ , ϵ and ζ [Hägg, 1931]; [Gulbransen & Andrew, 1954]; [Vaughan & Bridge, 1956]; [Beck, 1962]; [Zhao et al, 2008]:

- The most commonly reported hydride is face-centred-cubic with a space group of $Fm\bar{3}m$. It has a composition variously reported but usually between $MH_{1.5}$ and $MH_{1.67}$ and a lattice parameter at room temperature of 0.478 nm. It is designated the δ -phase. Usually the close packed planes and close packed directions of hydride and Zr are parallel providing the relationship between the hydride and the zirconium matrix of $(111)_{\text{hydride}}$ parallel with $(0001)_{\text{Zr}}$ and $[1\bar{1}0]_{\text{hydride}}$ parallel with $[11\bar{2}0]_{\text{Zr}}$ [Bradbrook et al, 1972]. In Zr alloys, the habit plane approaches the basal plane, often $(10\bar{1}7)$, [Westlake, 1968], which is about 14.7° from the basal plane.
- The hydride may take the form of a precipitate with a face-centred-tetragonal ($c/a > 1$) structure with a space group of $P4_2/n$ or $I4m_2$ [Christensen et al, 2015]. The composition is MH and the lattice parameters at room temperature are $a = 0.460$ nm and $c = 0.497$ nm. It is designated the γ -phase.
- At high concentrations of hydrogen, $MH_{1.67}$ to MH_2 , a face-centred-tetragonal ($c/a < 1$) structure appears with a space group of $I4/m$. The lattice parameters at room temperature are $a = 0.498$ nm and $c = 0.445$ nm. It is designated the ϵ -phase.
- A transient hydride phase has been reported that is a precursor to γ - or δ -hydrides. This metastable phase is called ζ -hydride. It has a composition of $ZrH_{0.25-0.5}$ and an hcp structure with $a = 0.33$ nm and $c = 1.03$ nm, with a space group of $P3m1$.

Hydrogen has a stabilizing effect on the β -phase with much solubility in this phase but a very low solubility limit in the α -phase, the most common phase in commercial alloys, Figure 10-2. As a result, detailed knowledge of the $\alpha/(\alpha+\text{hydride})$ boundary is required to understand and guard against hydride cracking in the temperature range in which components usually operate in nuclear reactors and with the hydrogen concentrations usually encountered. Much effort has been expended to determine this phase boundary. Some experimental methods are dynamic and the solubility limit appears different on heating and cooling. These methods include dilatometry [Erickson & Hardie, 1964], internal friction [Bungardt & Preisendanz, 1960], differential scanning calorimetry [Tashiro, 1993], and diffraction of x-rays [Colas et al, 2010], and neutrons [Root & Fong, 1996].

During heating of zirconium containing hydrides the concentration of hydrogen in solution gradually increases and the amount of hydride phase decreases until a temperature is reached where no hydrides are present. This temperature, T_D (K), increases with the concentration of hydrogen, C_D (ppm), and is usually described by the following equation:

$$\text{Eq. 10-1:} \quad C_D = A \exp(-\Delta H_D/RT_D)$$

where A is a constant, ΔH_D is the enthalpy of solution (kJ/mol) and R is the Gas Constant, 8.314 J/(K.mol).

Typical values are $A = 8.19 \times 10^4$ and $\Delta H_D = 34.5$ kJ/mol. The very low solubility limit is incontrovertible for all alloys, and as a result, with any practical specification and fabrication process, hydrides will always be present at room temperature in fresh components. At the limit allowed by the current technical specification for as-fabricated pressure tubes, 5 ppm (0.045 at. %), hydrides would be present up to 155°C. For as-fabricated fuel cladding, the maximum concentration allowed is 25 ppm (0.228 at. %) and at the limit, hydrides would be present up to 240°C.

During cooling from above T_D the metal has an apparent greater capacity to hold hydrogen in solution than after heating to the same temperature from, for example, room temperature, consequently the temperature at which hydrides precipitate is lower than the temperature at which the hydrides dissolve. The temperature dependence is represented similarly to Eq. 10-1:

$$\text{Eq. 10-2:} \quad C_P = B \exp(-\Delta H_P/RT_P)$$

where C_P represents the concentration of hydrogen where hydrides start to precipitate at temperature T_P .

Typical values for B and ΔH_P are 4.11×10^4 and 28 kJ/mol with the consequence that at temperatures up to 400°C the temperature for dissolution, T_D , appears to be 50 to 60°C greater than that for precipitation, T_P . This apparent hysteresis is always observed in dynamic experiments. For thermodynamic equilibrium, according to the Phase Rule, composition and temperature cannot be changed independently for two phases to be present in a binary alloy. At the same composition, hydrides should dissolve and precipitate at the same temperature independent of heating or cooling. The presence of two values of the solubility limit indicates that one or both the values do not represent equilibrium and the hysteresis and values are therefore indicated as “apparent”. In dynamic measurements, values of apparent TSS by heating or cooling are clearly distinguishable and reproducible even if strictly invalid as equilibrium values.

The solubility limit is not much affected by alloying additions and is independent of hydrogen isotope. Some measurements indicate that neutron irradiation increases C_d and C_p by a small amount although the size of the effect is controversial [McMinn et al, 2000]; [Vizcaino et al, 2002].

11 Irradiation induced changes of the crystal structure

Another important aspect is the **irradiation induced change of the Zr crystal structure** that results in irradiation hardening. During exposure in reactor substantial microstructural changes can occur, such as (1st) alloying element redistribution between the α -solid solution and the secondary phase precipitates, as discussed in Section 9.2 for Zircaloy and section 5 for Zr2.5Nb, (2nd) recrystallization of not-recrystallized grains, and (3rd) nucleation and evolution of dislocation loops³.

An important type of defect, particularly for irradiated materials, is the **dislocation loop**. If a significant number of vacancies or interstitials condense on a particular plane, a disk is formed with its boundary defined by a (circular) edge dislocation. This process is illustrated in Figure 11-1, [Franklin et al, 1983]. The Burgers vector \underline{b} is perpendicular to the plane of the loop and therefore is the normal to the plane on which the loop lies.

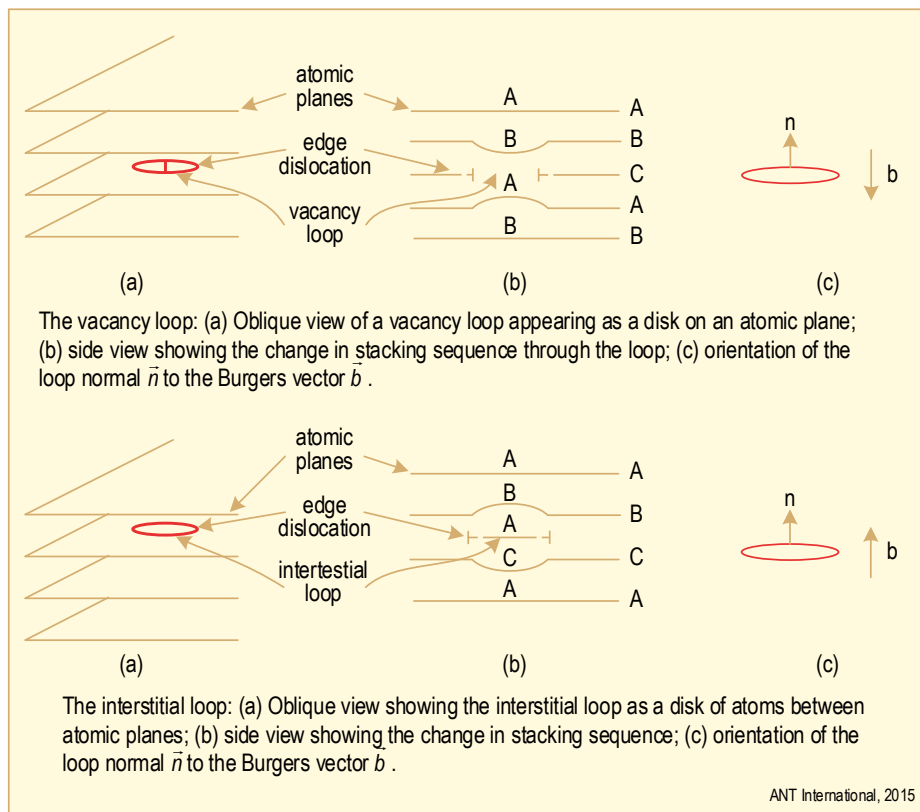


Figure 11-1: a) Vacancy loop and b) Interstitial loop, modified figure according to [Franklin et al, 1983].

Irradiation bombardment in the hexagonal Zr lattice results in the formation of self-interstitial atoms (SIAs), vacancies (V), and clusters of SIAs and V which diffuse until they become absorbed on lattice defects (sinks). In Zr alloys diffusional anisotropy difference causes SIAs to have a strong preference to diffuse parallel to the basal plane (in an $\langle a \rangle$ direction), whereas vacancy diffusion is more isotropic e.g. [Woo, 1988], [Christensen et al, 2015]. The interstitials produced by the neutron flux migrate preferentially to sinks with large dilatational strain fields, such as edge dislocations and loops whereas the net flux of vacancies arrive at neutral sinks such as grain boundaries and screw dislocations [Gilbert & Holt, 1981], see Figure 11-2.

³ In this section and in Section 9.2, we have mixed use of n/cm^2 and n/m^2 . $n/\text{cm}^2 = n/\text{m}^2/10^4$

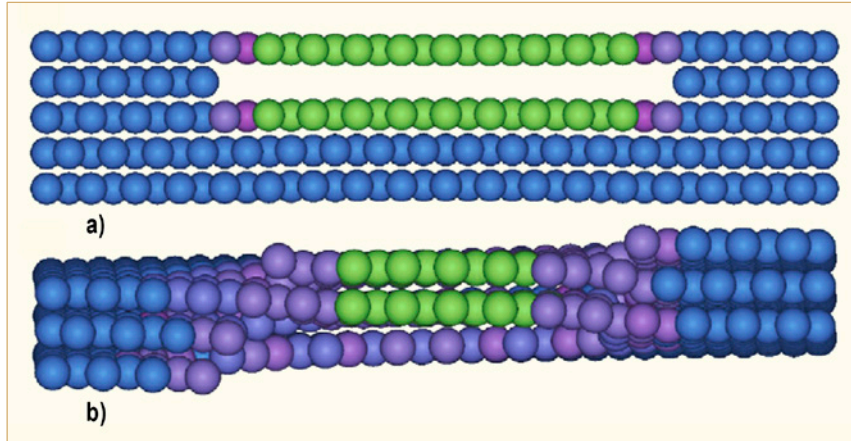


Figure 11-2: Change in the atomistic configuration of an 85-vacancy cluster platelet on the basal plane, (a) in the absence of the screw dislocation, and (b) in the presence of the $\langle c \rangle$ -screw dislocation. In the presence of the screw dislocation, it collapses into a stacking-fault. Atoms coloured green have the largest slip vectors and experience the largest lattice distortion around them, while those coloured blue have the smallest slip vector with the smallest lattice distortion [Woo & Xiangli, 2009].

The diffusion anisotropy and the sink preference of SIAs results in a preferential vacancy migration to $\langle c \rangle$ -screw dislocations and loops. The consequence of these preferences is a shrinkage of the grains in the $\langle c \rangle$ $\langle 0001 \rangle$ direction (irradiation growth in the $\langle a \rangle$ direction).

Irradiation modifies the dislocation structure through nucleation and growth of dislocation loops. In detail these changes depend significantly on the initial condition. For cold-worked materials in particular, climb of existing network dislocations proceeds. Before irradiation a high density of deformation-induced $\langle a \rangle$ -component and mixed $\langle a+c \rangle$ dislocations are present in the CWSR material while completely recrystallized grains with few dislocations are in the RX material. In 25% cold worked Zr alloys the $\langle c \rangle$ -component network dislocation density is increased by irradiation, e.g., at $\sim 60^\circ\text{C}$ to 7×10^{21} n/cm², as Figure 11-3 shows from 4×10^9 to 8×10^9 per-cm². The development of basal plane $\langle c \rangle$ -component dislocation segments (by helical climb) is also observed at 280-310°C in cold-worked Zr-2. As with the low temperature case, this behaviour is explained by helical climb on pre-existing $\langle c \rangle$ -component screw dislocations [Griffiths et al, 1996].

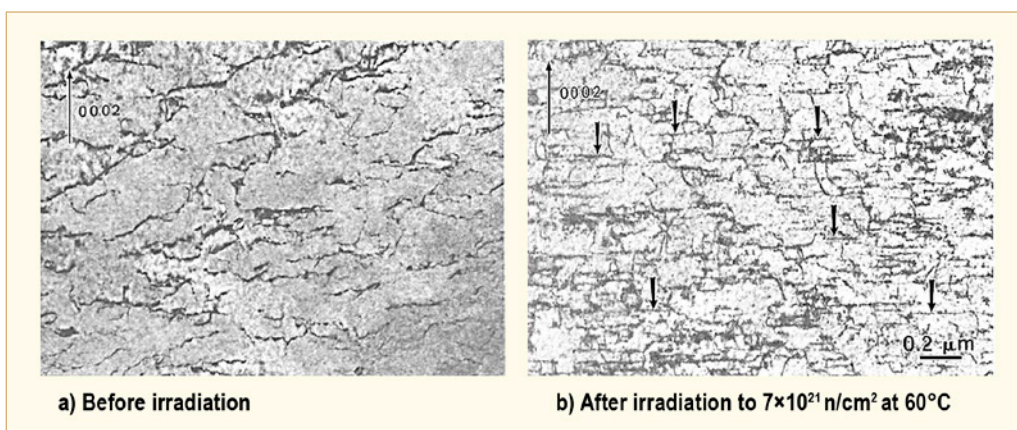


Figure 11-3: Comparison of $\langle c \rangle$ -type dislocation structures in Zircaloy-2 (a) before and (b) after irradiation to a fluence of 7×10^{21} n/cm² at about 60°C. Edge segments (arrowed) are produced during irradiation [Griffiths et al, 1996]

In all Zr alloys under irradiation dislocation loops are formed. Two types of loop structures appear in Zr alloys: loops with $\langle a \rangle$ -type Burgers vector and loops with $\langle c \rangle$ -component Burgers vector (Figure 11-4). The $\langle a \rangle$ -loop lies on a prism plane. Both interstitial and vacancy $\langle a \rangle$ -loops are formed, but the relative proportions of each type are determined by the irradiation temperature and the presence of other microstructural features (grain boundaries, network dislocations, $\langle c \rangle$ - loops, etc.). The $\langle c \rangle$ type of loop lies on the basal plane. Unlike the $\langle a \rangle$ loop, it is strictly a vacancy-type loop, is relatively large (100 nm), and does not form until irradiation doses become high.

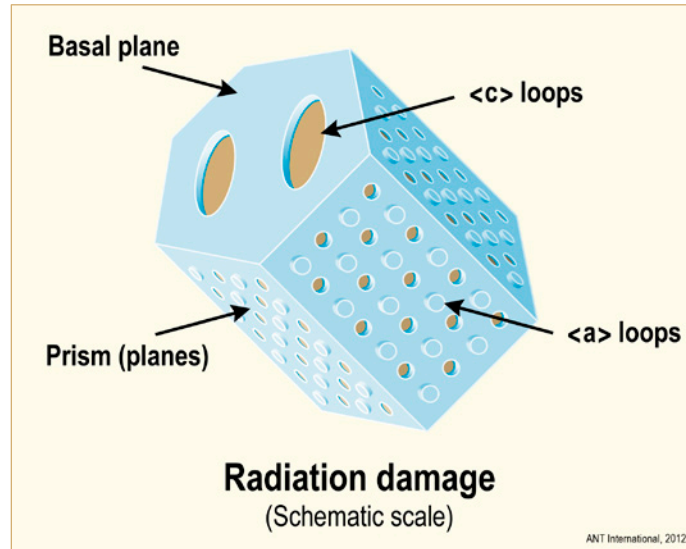


Figure 11-4: Schematic view of the $\langle a \rangle$ and $\langle c \rangle$ loops.

Their size and density are primarily dependent on the irradiation temperature. For annealed Zircaloy-2 irradiated at $\sim 60^\circ\text{C}$ (e.g. calandria tubes in CANDU reactors), the radiation damage creates $\langle a \rangle$ -type loops that are < 5 nm in diameter. Their density increases from about 0.1 (as-received) to about 1×10^{14} per m^2 after a fluence of about 3×10^{21} n/cm^2 . There is no significant increase of the $\langle c \rangle$ -component dislocation density (typically remaining within the range of 0.01 to 0.1×10^{14} per m^2), and no $\langle c \rangle$ -component loop formation up to about 2.5×10^{22} n/cm^2 at $\sim 60^\circ\text{C}$.

For the same type of alloy operating at about 300°C (Zircaloy-4 guide tubes in PWRs and channel boxes in BWRs), the $\langle a \rangle$ -type loops are larger, about 10 to 20 nm in diameter, and formed at low fluences, at $\leq 1 \times 10^{21}$ n/cm^2 . Their density increases from about 0.1 (as-received) to about 8×10^{14} per m^2 . The higher apparent $\langle a \rangle$ -type dislocation density at the higher temperature, compared with material irradiated at about 60°C , may reflect differences in the strain fields from the bounding dislocations. A typical TEM photo of $\langle a \rangle$ -loops can be seen in Figure 11-5a between dislocations. The $\langle a \rangle$ -loops form early in the irradiation and the number density reaches a saturation value at a neutron fluence less than 0.5×10^{21} n/cm^2 (Figure 11-6). Their size number density is almost independent on the alloy type (Zircaloy-2/4, Zr2.5Nb, Zr1Nb, Zr1Sn1NbFe alloys). The size of the loops increases and their density decreases with increasing irradiation temperature in the range 250 - 320°C , and the loops become unstable (start to disappear) at about 400°C . They have a strong effect on mechanical properties, as will be discussed in Section 12.

12 Effect of irradiation on properties

12.1 Mechanical properties

Knowledge of the effects of in-reactor environment on tensile and fracture properties, and on deformation, is important for judging the fitness-for-service of components. Two methods are used to evaluate the effects of neutron irradiation on the mechanical properties of materials – unirradiated test specimens are placed inside a test or power reactor and tested out-reactor or test specimens are machined out of components that have been in-service in power reactors. In the latter, the irradiation conditions are the industrial environment and are known, but the control of the irradiation conditions is not as precise as in a test reactor. Short-term mechanical tests are rarely done in-reactor.

Zirconium alloys exhibit an increase in strength after irradiation, usually combined with a reduction of ductility. The mechanisms involve the dislocation loops produced by the irradiation, Section 11, which act as barriers for the motion of the mobile dislocations. Above the yield stress, once plastic deformation has started, the mobile dislocations react with the loops, annihilating them in narrow bands, Figure 12-1 [Regnard et al, 2002]. After a low plastic strain, this localisation of deformation leads to strain softening. These behaviours are illustrated for pure Zr irradiated at 80°C and tested at 25°C, Figure 12-2 [Byun et al, 2004]. An increase in yield strength of about 110 MPa is induced by an irradiation damage dose as low as 0.1 dpa (5×10^{23} n/m²).

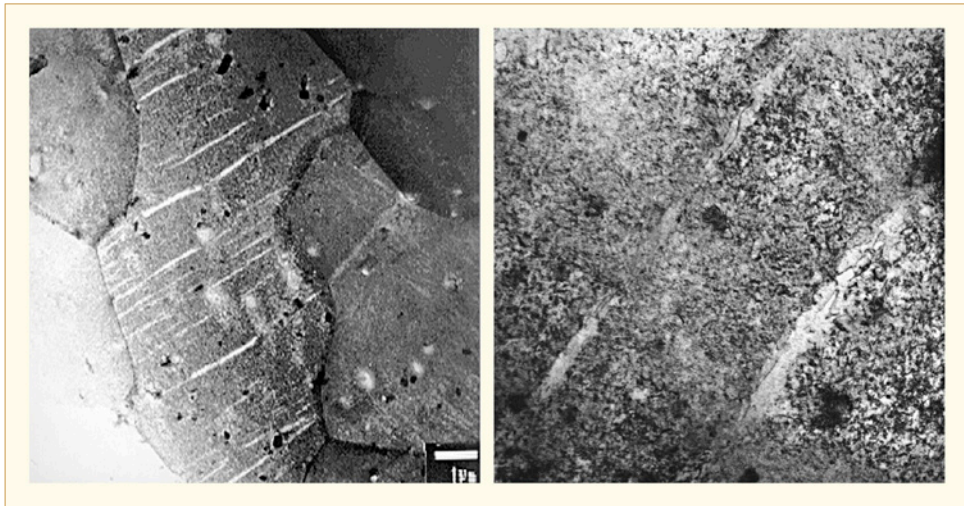


Figure 12-1: Channels cleared of irradiation damage in Zircaloy-4 strained 0.8% after neutron irradiation at 300°C [Regnard et al, 2002].

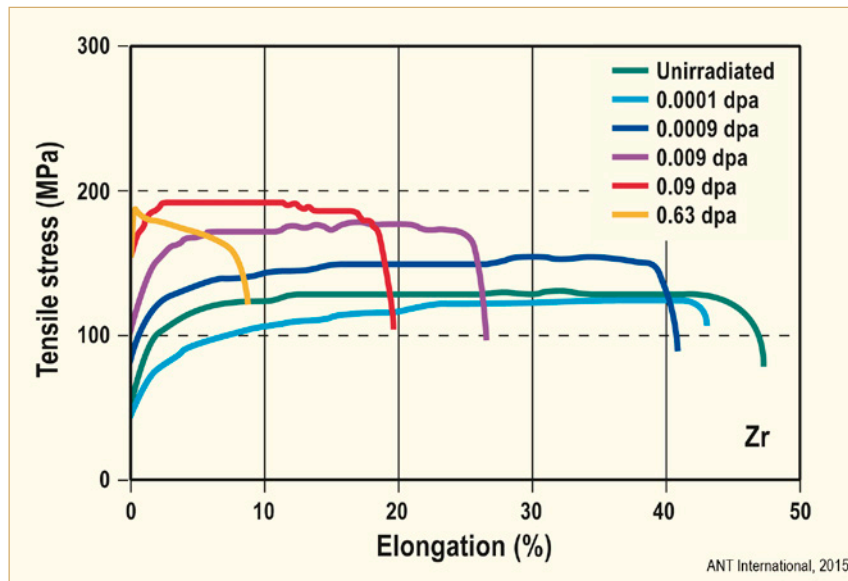


Figure 12-2: Effect of neutron irradiation at 80°C on the tensile properties of pure zirconium tested at 25°C, after [Byun et al, 2004].

For the conditions relevant to power reactor operation with temperatures in the range of 250 – 350°C and doses up to 20 dpa (10^{26} n/m²), a consistent qualitative picture has emerged for all zirconium alloys:

- The strength increases about 200 MPa up to a fluence of about 3×10^{24} n/m². This strengthening corresponds to between a 10 and 300% increase, the larger proportional increase is obtained with weak starting materials and vice versa. The transient is followed by a gradual increase in strength with neutron fluence, Figure 12-3 [Cappelaere et al, 2002].
- The initial transient corresponds with the early increase in <a>-type dislocation density that saturates at a low fluence, Figure 11-6 The additional hardening is attributed to the continuous increase in <c>-type loop density [Pan et al, 2005], which may not saturate, Figure 11-7.
- Recrystallized and CWSR materials will exhibit similar strengths after an irradiation dose of about 10^{25} n/m². A reduction of the anisotropic behaviour is observed after irradiation; the plane strain/tensile strength ratio becomes close to isotropic behaviour after irradiation [Tomalin, 1977] while the same effect was observed with Knoop hardness tests on irradiated materials, [Nakatsuka & Nagai, 1987]. The results were analysed as an increased resolved shear stress on the prismatic slip planes allowing new gliding systems to be activated, including basal slip.
- As the irradiation temperature is increased beyond 360°C, the irradiation damage starts to anneal out as fast as it is produced and the hardening diminishes. This high temperature response is strongly affected by neutron flux, with a high flux raising the temperature for no hardening.

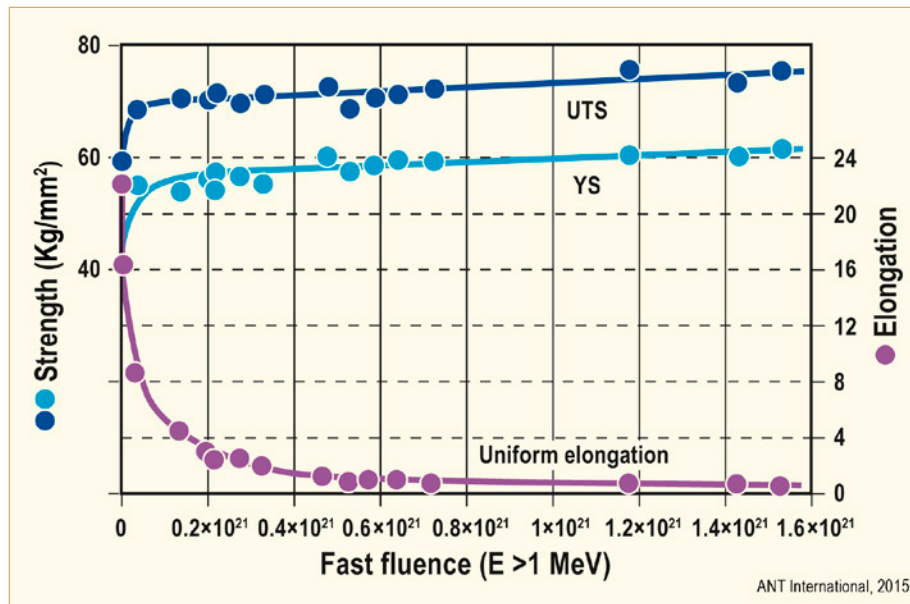


Figure 12-3: Irradiation hardening of Zircaloy-4 irradiated at 320–360°C (dose in n/cm^2), after [Cappelaere et al, 2002].

A consequence of the annihilation of irradiation damage during straining is a localisation of the deformation in intense bands of deformation. This deformation leads to a reduction in load-carrying capacity and strain softening and a reduction of the strain to maximum load, for example, curve for 0.63 dpa in Figure 12-2. The clearing process depends on irradiation conditions, amount of strain, test temperature, and material texture, composition and microstructure. Irradiation damage locks the sources of mobile dislocations and a high stress is required to activate them – hence irradiation strengthening. Once activated, avalanches of dislocations sweep away the irradiation barriers and create a stress concentration at a grain boundary or is restricted by other microstructural features, such as dislocation cell structures in cold-worked material. The tendency to form channels increases as the yield strength of the material rises with amount of irradiation leading to a threshold fluence. For example, a threshold fluence for the formation of channels was indicated in annealed Zircaloy-2 irradiated between 150 and 200°C; after deformation at 320°C material irradiated to 3.0×10^{24} n/m^2 contained channels whereas material irradiated to 3.2×10^{23} n/m^2 did not [Onchi et al, 1983]. Channels free of irradiation damage are observed before their effect is manifest on a macro-scale as a load drop [Onimus et al, 2004]. Since less force is required to maintain further deformation after the initial channels are formed, new sources of dislocations are difficult to activate in the surrounding strong material in the original grain and the increase in the number of channels declines with further macrostrain. The deformation is heterogeneous; in annealed alloys tested at 350°C, between 40 and 60% of the grains contained narrow channels. The widths of the channels and their spacing appear to have a weak dependence on the irradiation fluence, but none on test temperature or plane of the channel. The confined strain within the channels can be very high, over 100% [Williams et al, 1974], producing high stresses at the grain boundaries that may lead to new channels in the adjacent grains, and displacement at the boundaries [Lee & Adamson, 1977] or surfaces. As the material is deformed, the original channels work-harden and dislocation cells form in material free of irradiation damage [Coleman et al, 1972]. Subsequent deformation continues to be restricted and appears as shear bands that are visible to the naked eye on the surface, Figure 12-4, [Byun & Farrell, 2004]. Most of the observations on clearing out irradiation damage are on annealed Zircaloy. Irradiation damage is also annihilated in cold-worked materials during deformation but the channels are much less obvious and the original dense dislocation structure both impedes their development and obscures their observation. Channelling in β -quenched or welded Zircaloy is also obstructed by the Widmanstätten structure, or grain-to-grain variation in texture, or both. Additional information on channelling is given in Section 6.2.

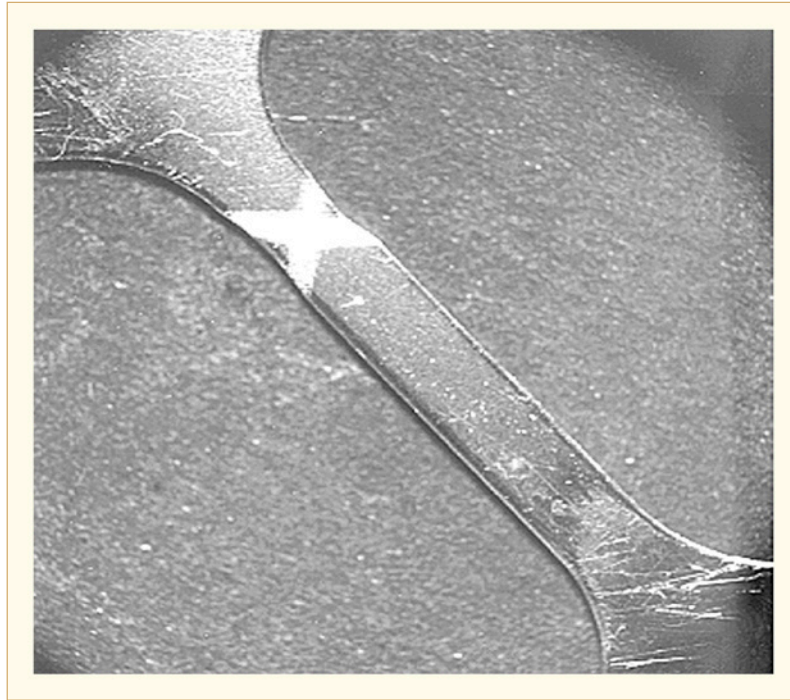


Figure 12-4: Localized strain in a tensile sample of Zircaloy-4 strained 0.8% at 350°C after irradiation to 6×10^{24} n/m² at 280°C [Byun & Farrell, 2004].

The decrease in uniform elongation caused when irradiation damage is annihilated is especially large in material that starts out in the annealed condition. The subsequent amount of elongation before rupture, the necking strain, is decreased because the effective gauge length of specimens is reduced by the localisation of the deformation. The total elongation is thus much reduced. The reduction in the uniform strain by irradiation is not much affected by test temperature but the remnants of cold-work ameliorate the severity of the loss in the ability to hold a load. This effect reflects channelling being obstructed by the forest dislocations. The necking strain is also much reduced by irradiation in annealed material but less so in CWSR material.

Any model of the stress-strain-strain rate history of irradiated zirconium alloys should include:

- strengthening,
- clearing of irradiation damage before any effect on the load-carrying capacity is detected,
- clearing of irradiation damage in several grains, perhaps forming a dominant slip region, leading to a loss in load-carrying capacity,
- dislocation accumulation and work-hardening of the zones cleared of irradiation damage,
- a loss in elongation,
- identifying the primary channelling plane, e.g... prism or basal or others.

Several attempts include some of these features [Hosbons et al, 1975], [Lee & Adamson, 1977], [Onimus et al, 2004], [Onimus & Béchade, 2009] and are cited for further interest.

14 References

- Abe H. et al., *Deformability of Zr-Lined Cladding tube in Cold pilgering*, ASTM STP 1132, pp. 34-47, 1991.
- Abriata J. P. and Bolcich J. C., *Nb-Zr (Niobium-Zirconium)*, Binary Alloy Phase Diagrams, Second edition, T.B. Massalski, Ed., 3, pp. 2788-2789, 1990.
- Adamson R. B., *Irradiation Growth of Zircaloy*, Zirconium in the Nuclear Industry; Third Conference, ASTM STP 633, pp. 326, 1977.
- Adamson R. B. and Bell W. L., *Effects of Neutron Irradiation and Oxygen Content on the Microstructure and Mechanical Properties of Zircaloy*, Microstructure and Mechanical Behavior of Materials, Proceedings: Int'l Symposiums, Xian, China, October, 1985, EMAS, pp. 237-246, Warley, UK, 1986.
- Adamson R. B. and Lewis J. L., Abstracts, Ninth International Symposium, Zirconium in the Nuclear Industry, Kobe, Japan, 1991.
- Adamson R. B., *Alloy for improved corrosion resistance of nuclear reactor components*, Patent EP0735151B1, 1996.
- Adamson R. B., *Effects of neutron irradiation on microstructure and properties of Zircaloy*, ASTM STP 1354, pp. 15-31, 2000.
- Adamson R. B., Cox B., Garzarolli F., Strasser A., Rudling P. and Wikmark G., *Corrosion of Zirconium Alloys*, ZIRAT7/IZNA2 Special Topics Report, ANT International, Mölnlycke, Sweden, 2002.
- Adamson R. B. and Cox B., *Impact of Irradiation on Material Performance*, ZIRAT10/IZNA5 Special Topics Report, ANT International, Mölnlycke, Sweden, 2005.
- Adamson R. B., *recovery of irradiation damage by post-irradiation thermal annealing: relevance to hydrogen solubility and dry storage issues*, EPRI, Palo Alto, CA., Report 1013446, 2006.
- Adamson R., Garzarolli F., Cox B., Strasser A. and Rudling P., *Corrosion Mechanisms in Zirconium Alloys*, ZIRAT12/IZNA7 Special Topics Report, ANT International, Mölnlycke, Sweden, 2007.
- Adamson R. B., Garzarolli F., Patterson C., Rudling P. and Strasser A., *ZIRAT14/IZNA9 Annual Report*, ANT International, Mölnlycke, Sweden, 2009a.
- Adamson R. B., Garzarolli F. and Patterson C., *In-Reactor Creep of Zirconium Alloys*, ZIRAT14/IZNA9 Special Topical Report, ANT International, Mölnlycke, Sweden, 2009b.
- Adamson R. B., Garzarolli F., Patterson C., Rudling P. Strasser A. and Coleman K., *ZIRAT15/IZNA10 Annual Report*, ANT International, Mölnlycke, Sweden, 2010.
- Adamson R., Garzarolli F., Patterson C., Rudling P., Strasser A., Coleman K. and Lemaignan C., *ZIRAT16/IZNA11 Annual Report*, ANT International, Mölnlycke, Sweden, 2011.
- Adamson R. B., Coleman K., Mahmood S. T. and Rudling P., *Mechanical Testing of Zirconium Alloys, Volume 1*, ZIRAT18/IZNA13 Special Topic Report, ANT International, Mölnlycke Sweden, 2013.
- Akhtar A. and Teghtsoonian A., *Basal Slip in Zirconium*, Acta Met., Vol. 19, pp. 655, 1971.
- Akhtar A., *Basal slip in zirconium*, Acta Met. Vol. 21, pp. 1-11, 1973a.

- Akthar A., *Compression of Zr single crystals parallel to c axis*, J. Nucl. Mat. 47, pp. 79-86, 1973b.
- Alam A. M. and Hellwig C., *Cladding tube deformation test for stress reorientation of hydrides*, J. ASTM International, 5, Paper ID JAI101110, 2008.
- Andersson T. et al., *Influence of thermal processing and microstructure on the corrosion behavior of Zircaloy-4 tubing*, IAEA SM 288/59. IAEA, Vienna, 1986.
- Anonymous, *Standard specification for wrought zirconium alloy seamless tubes for nuclear reactor fuel cladding*, ASTM International, B811-07 (Approved 2007).
- Ashby M. R., *Philosophical Magazine*, Vol. 21, p. 399, 1970.
- Asher R. C. and Trowse F. W., *The distribution of hydrogen in zirconium alloy fuel cladding: the effect of heat flux*, J. Nucl. Mater., 35, pp. 115-121, 1970.
- Averin S. A., Panchenko V. L., Kozlov A. V., Sinelnikov L. P. Shishov V. N. and Nikulina A. V., *Evolution of dislocation and precipitate structure in Zr alloys under long term irradiation*, ASTM STP 1354, pp. 105-121, 2000.
- Avril J., *Encyclopedie Vishay d'anlyse des contraintes*, Malakoff, Paris, France, 1974.
- Bajaj R., Kammenzind B. F., and Farkas D. M., *Effects of Neutron Irradiation on the Microstructure of Alpha-Annealed Zircaloy-4*, Zirconium in the Nuclear Industry: 13th International Symposium, ASTM STP 1423, Eds. G. D. Moan and P. Rudling, ASTM International, pp. 400-426, West Conshohocken, PA, 2002.
- Ballinger R. G. et al., *The effect of plastic strain on the evolution of crystallographic texture in Zircaloy-2*, J. Nucl. Mat. 126, p. 53-69, 1984.
- Barb ris P., Charquet D and Rebeyrolle V., *Ternary Zr-Nb-Fe(O) System: Phase Diagram at 853 K and Corrosion Behaviour in the Domain Nb<0.8%*, J. Nucl. Mater., Vol. 326, pp. 163-174, 2004.
- Barb ris P., Dupin N., Lemaignan C., Pasturel A. and Grange J. M., *Microstructure and Phase Control in Zr-Fe-Cr-Ni Alloys: Thermodynamic and Kinetic Aspects*, Journal of ASTM International, Vol. 2 (5), paper JAI12771, pp. 129-156, 2005.
- Beck R. L., *Zirconium-hydrogen phase system*, Trans. ASM, 55, pp. 542-555, 1962.
- Bell W. L., Discussion, *Zirconium in Nuclear Applications*, ASTM STP 551, pp. 199-120, 1974.
- Bement A. L., Jr., *Radiation Effects*, AIME Metallurgical Society Conferences, Vol. 37, Ed. W. F. Sheely, pp. 671, 1967.
- Billone M. C., Burtseva T. A. and Einziger R. E., *Ductile-to-brittle transition temperature for high-burnup cladding alloys exposed to simulated drying-storage conditions*, J. Nucl. Mater., 433, pp. 431-448, 2013.
- Bingert J. et al., *Deformation twinning in polycrystalline Zr: Insights from electron backscattered diffraction characterization*, Metallurgical and Materials Transactions A, Volume 33, Number 13, pp. 955-963(9), Publisher: Springer, March 2002.
- Bourdilliau B. et al., *Impact of irradiation damage recovery during transportation on the subsequent room temperature tensile behavior of irradiated zirconium alloys*, 16th International Symposium on Zirconium in the Nuclear Industry, ASTM, Chengdu, China, May, 2010.
- Bradbrook J. S., Lorimer G. W. and Ridley N., *The precipitation of zirconium hydride in zirconium and Zircaloy-2*, J. Nucl. Mater., 42, pp. 142-160, 1972.